Comprehensive mapping of sensory and sympathetic innervation of the developing kidney

Pierre-Emmanuel Y. N'Guetta[1], Sarah R. McLarnon[1], Adrien Tassou[2], Matan Geron[2], Sepenta Shirvan[3], Rose Z. Hill [3], Grégory Scherrer[4], Lori L. O'Brien[1*]

[1]Department of Cell Biology and Physiology, The University of North Carolina at Chapel Hill, Chapel Hill, NC 27599, USA

[2]Department of Cell Biology and Physiology, UNC Neuroscience Center, Department of Pharmacology, The University of North Carolina at Chapel Hill, Chapel Hill, NC 27599, USA

[3]Department of Neuroscience, Dorris Neuroscience Center, The Scripps Research Institute, La Jolla, CA, USA 92037

[4]Department of Cell Biology and Physiology, UNC Neuroscience Center, Department of Pharmacology, The University of North Carolina at Chapel Hill, Chapel Hill, NC 27599, USA; New York Stem Cell Foundation – Robertson Investigator, The University of North Carolina at Chapel Hill, Chapel Hill, NC 27599, USA

*Corresponding author: lori_obrien@med.unc.edu

Keywords: Innervation, nerve, kidney development, sympathetic, sensory

Abstract

The kidney functions as a finely tuned sensor to balance body fluid composition and filter out waste through complex coordinated mechanisms. This versatility requires tight neural control, with innervating efferent nerves playing a crucial role in regulating blood flow, glomerular filtration rate, water and sodium reabsorption, and renin release. In turn sensory afferents provide feedback to the central nervous system for the modulation of cardiovascular function. However, the cells targeted by sensory afferents and the physiological sensing mechanisms remain poorly characterized. Moreover, how the kidney is innervated during development to establish these functions remains elusive. Here, we utilized a combination of light-sheet and confocal microscopy to generate anatomical maps of kidney sensory and sympathetic nerves throughout development and resolve the establishment of functional crosstalk. Our analyses revealed that kidney innervation initiates at embryonic day (E)13.5 as the nerves associate with vascular smooth muscle cells and follow arterial differentiation. By E17.5 axonal projections associate with kidney structures such as glomeruli and tubules and the network continues to expand postnatally. These nerves are synapsin I-positive, highlighting ongoing axonogenesis and the potential for functional crosstalk. We show that sensory and sympathetic nerves innervate the kidney concomitantly and classify the sensory fibers as calcitonin gene related peptide (CGRP)$^{+}$, substance P^{+}, TRPV1^{+}, and PIEZO2^{+}, establishing the presence of PIEZO2 mechanosensory fibers in the kidney. Using retrograde tracing, we identified the primary dorsal root ganglia, T10-L2, from which PIEZO2^{+} sensory afferents project to the kidney. Taken together our findings elucidate the temporality of kidney innervation and resolve the identity of kidney sympathetic and sensory nerves.

63

64 **Introduction**

65 Major functions of the kidney include the maintenance of body fluid and electrolyte
66 homeostasis and modulation of blood pressure. These functions are maintained by a
67 variety of intrinsic cellular mechanisms as well as extrinsic input from the nervous system
68 (May et al., 2010; McMahon, 2016; Osborn et al., 2021). Peripheral neurons originating
69 from ganglia innervate the kidney and are predominantly unmyelinated C-fibers (Kneupfer
70 and Schramm, 1987; Booth et al., 2015; Osborn et al., 2021), although some myelinated
71 renal afferent fibers have been reported in the kidney, yet their identity remains unclear
72 (Simon and Schramm, 1983; Kneupfer and Schramm, 1987; Stella and Zanchetti, 1991).
73 Kidney innervation consists of afferent sensory nerves that influence cardiovascular
74 function through the relay of chemical and mechanical information from the kidney to the
75 central nervous system (CNS), or efferent sympathetic nerves regulating renal function
76 through the CNS (Osborn et al., 2021). Precise innervation and modulation of nerve
77 activity maintains kidney physiology while aberrant nerve function is associated with
78 several kidney diseases (DiBona & Kopp, 1997; Malpas, 2010; Sata et al., 2018).
79 Therefore, modulating nerve activity is widely seen as a potential therapy to address
80 kidney-related physiological disorders (Bhatt et al., 2022). Yet, to achieve such precise
81 neuromodulation, an accurate mapping of the kidney nerve origins and a complete
82 understanding of their molecular identity is necessary. Many studies to date have focused
83 on sympathetic nerves and their regulation of mature kidney physiology. Therefore, we
84 still lack detailed information about how both the sensory and sympathetic innervation of
85 the kidney is established and how nerves pattern to reach their target cells and establish
86 crosstalk.

87 Sympathetic nerves participate in the control of several kidney functions including
88 vascular tone and glomerular filtration rate, sodium and water reabsorption, and renin
89 release (Denton et al., 2004; DiBona, 2000; Fujisawa et al., 2011). They also modulate
90 processes such as the release of cytokines to mediate inflammatory responses (Banek
91 et al., 2016; Osborn et al., 2021; Veelken et al., 2008; Xiao et al., 2015). Overactivity of
92 kidney sympathetic nerves contributes to the development and maintenance of
93 hypertension (Osborn et al., 2021; Sata et al., 2018). In contrast to the numerous

94 functions for sympathetic nerves in both normal physiology and pathophysiology, our
95 understanding of kidney sensory nerve anatomy, classification, and their physiological
96 roles remain poorly understood (Osborn et al., 2021). Kidney sensory nerves have been
97 thus far been classified as transient receptor potential cation channel subfamily V member
98 1-positive (TRPV1^{+}) due to their response to capsaicin and have also been shown to
99 produce the nociceptor-associated neuropeptides calcitonin gene-related peptide
100 (CGRP) and substance P (Osborn et al., 2021; Tyshynsky et al., 2023). Sensory neurons
101 innervating the kidney project to the dorsal horn and synapse onto interneurons that
102 project to CNS sites regulating cardiovascular function and in turn feedback to modulate
103 kidney sympathetic nerve activity (Kopp, 2015). Recently, studies have established the
104 importance of mechanosensitive PIEZO2 sensory nerves in the urogenital system to
105 regulate bladder and sexual function (Lam et al., 2023; Marshall et al., 2020). However,
106 whether PIEZO2 sensory nerves are also present in the kidney is unknown. Lastly, a
107 recent study published by Cheng et. al. show parasympathetic cholinergic (ChAT^{+} and
108 VAChT^{+}) nerves innervate the renal artery and pelvis with cholinergic ganglion found
109 within the kidney nerve plexus (Cheng et al., 2022). Whether these axons project to the
110 kidney cortex and associate with cells or structures within kidney has not been elucidated
111 to date. Initial studies of renal denervation in hypertensive patients led to a decrease in
112 blood pressure although further intensive trials reported that certain patients experienced
113 a rise in arterial pressure (Krum et al., 2013, 2014; Osborn & Foss, 2017; Schlaich et al.,
114 2009; Symplicity HTN-2 Investigators et al., 2010; Townsend et al., 2017). To date, this
115 method of controlling hypertension remains an attractive option with additional trials being
116 conducted. However, such procedures non-selectively target both sensory and
117 sympathetic nerves, therefore understanding the full extent of kidney nerve activity may
118 inform efforts to optimize renal denervation strategies.

119 Ganglia located externally send axonal projections to the kidney. It has been
120 reported that sympathetic innervation arises from the celiac, superior mesenteric,
121 aorticorenal ganglia, and partially from the paravertebral chain depending on the model
122 system being used (Barajas et al., 1992; Bell & McLachlan, 1982; Ferguson et al., 1986,
123 1988; Kuo et al., 1982). In rat, studies have shown that kidney sensory neurons project
124 from dorsal root ganglion (DRG) at level T6 to L4, the majority of which derive from DRG

125 at the level of T12–L3 (Donovan et al., 1983; Weiss & Chowdhury, 1998). However, the
126 origin of sensory axons which innervate the mouse kidney is unclear. Moreover, the
127 process of kidney innervation during development, in any model, has not been detailed
128 thoroughly aside from a few recent studies reporting the close association of nerves with
129 the developing kidney arterial tree (Honeycutt et al., 2023; Tarnick et al., 2023). In this
130 study, we provide detailed spatiotemporal mapping of mouse kidney sensory and
131 sympathetic neurons across embryonic and early postnatal development, as well as their
132 persistence in the adult. We establish when kidney innervation begins, origins in the DRG,
133 the spatial organization and growth of axons, their association with kidney cells and
134 structures, as well as the identity of the nerves across these different stages. Altogether,
135 we have generated a rich resource of knowledge surrounding kidney innervation that will
136 inform studies of both kidney development and physiological regulation.
137
138 **Results**
139 ***Spatiotemporal mapping of kidney innervation***
140 Due to the lack of knowledge on how kidneys are innervated during development,
141 we set out to determine when neuronal axons first reach the kidney and how this network
142 subsequently expands. We generated spatiotemporal maps of kidney innervation
143 throughout development by performing wholemount immunostaining followed by 3D light-
144 sheet imaging of either whole urogenital systems (E12.5, E13.5) or individual kidneys
145 (E14.5, E16.5, E18.5, P0, P7). Kidneys and urogenital systems were immunostained with
146 the pan-neuronal marker α-tubulin class III (TUBB3, TUJ1) to visualize axons, the arterial
147 marker α-smooth muscle actin (SMA), and the endothelial marker CD31. Our previous
148 studies have shown that the nerves and vasculature are tightly aligned in the developing
149 kidney, therefore we wanted to further examine the association of these two networks at
150 the various developmental timepoints (Honeycutt et al., 2023). Male and female kidneys
151 were both examined, with no significant differences observed, therefore the data
152 presented is representative of either sex. At E12.5, no TUBB3$^+$ nerves or SMA$^+$ vessels
153 could be identified in the kidney, which was discerned by cytokeratin staining of the
154 ureteric tree (**Fig. 1A; Movie S1**). SMA$^+$ cells were primarily localized to the descending
155 aorta with no SMA$^+$ vascular mural cells yet found in the kidney, correlating with previous

156 investigations of kidney vascularization **(Fig. 1A)** (Daniel et al., 2018). Despite the lack of
157 axons in the kidney, we did observe the presence of ganglia and postganglionic nerve
158 fibers tracking with the descending aorta (**Fig. 1A**). As organogenesis continues, TUBB3$^+$
159 nerve fibers navigate towards the kidney and begin innervation at E13.5, closely
160 associating with SMA$^+$ mural cells which mark the maturing renal arteries (**Fig. 1B,**
161 **arrowheads; Movies S2,S3**) (Daniel et al., 2018; Honeycutt et al., 2023; Luo et al., 2023;
162 Tarnick et al., 2023). Despite the low SMA$^+$ vascular mural cell coverage at this timepoint,
163 an extensive CD31$^+$ endothelial network is established in the kidney by E13.5 (**Fig. 1B**).
164 At E14.5, SMA coverage was more extensive, marking several arterial branches
165 (**Fig. S1A**). Concurrently, the TUBB3$^+$ nerve fibers continue tracking with the major
166 arterial branches, only extending along the portion of endothelium with SMA$^+$ vascular
167 mural cell coverage (**Fig. S1A**). Additionally, axons track with the SMA$^+$ ureteric smooth
168 muscle layer (**Fig. S1A)**. As development continues, axons grow and branch in
169 coordination with the arterial network, highlighting a tight neurovascular interplay as the
170 major arterial branches are established by E16.5 (**Fig. 1C; Movie S4**). Multiple nerve
171 fibers associate with a single arterial branch and the larger fibers may consist of multiple
172 axons which are tightly bundled (**Fig. 1C, arrowhead).** Once the major arterial branches
173 were established, the axonal network expanded via interstitial branching as observed at
174 E18.5 (**Fig. 1D; Movie S5**). The branching axons can be observed looping around
175 structures such as glomeruli (**Fig. 1D, arrowhead; Movie S5**). Subsequent imaging of
176 the postnatal kidney at postnatal day (P)0 (**Fig. S1B**) and P7 (**Fig. S1C**) revealed a
177 significant increase in nerve fiber density and arborization of the network due to continued
178 axonal growth and branching. Together, these data highlight the coordinated growth of
179 an extensive neuronal network as kidney organogenesis progresses.
180 To visualize the innervation of target cells and structures within the developing
181 kidney at greater resolution, we performed confocal imaging on E18.5 kidney sections.
182 Supporting our wholemount 3D analyses, we observed the axons tightly associating with
183 SMA+ vasculature, with several fibers often being associated with any one arterial branch
184 (**Fig. 2A**). The nerves track with renal arteries and arterioles into the renal cortex and can
185 separate from the SMA$^+$ vascular mural cells to loop around and associate with the
186 Bowman's capsule of glomeruli (**Fig. S2B, Fig. 1D**) and tubule epithelia (**Fig. S2C**).

187 Overall, kidney innervation is tightly linked to arterial differentiation with axons
188 dissociating from the SMA$^+$ vessels to navigate towards or around kidney target structures
189 such as glomeruli.
190
191 ***Sensory nerves innervate the developing kidney***
192 While we have mapped the spatiotemporal innervation of the developing kidney,
193 TUBB3 is a pan-neuronal marker labeling all nerve fiber types. It is well established that
194 the mature kidney is innervated by sympathetic neurons that modulate renal physiology,
195 however, the contribution of sensory nerves and the timing of sensory innervation in the
196 kidney is poorly understood (Kopp, 2015; Osborn et al., 2021). To visualize the
197 distribution and abundance of sensory neurons in the developing kidney, we crossed the
198 *Trpv1^{Cre}* line to the *Rosa(R)26^{tdTomato}* reporter line (*Trpv1$^{Cre/+}$;R26$^{tdTomato/+}$*) to label all
199 nociceptive TRPV1$^+$ sensory neurons. TRPV1$^+$ nociceptive neurons are thought to
200 comprise the majority of, if not all sensory nerves within the kidney and therefore labeling
201 this population should accurately represent the sensory contribution (Stocker & Sullivan,
202 2023; Tyshynsky et al., 2023). We performed wholemount imaging on
203 *Trpv1$^{Cre/+}$;R26$^{tdTomato/+}$* kidneys at E16.5 to visualize the total complement of sensory
204 nerve fibers traced from the start of kidney innervation. TdTomato$^+$ signal extensively
205 overlapped with the pan-neuronal marker TUBB3 (**Fig. 2A**). To visualize these sensory
206 fibers and their association with kidney structures in greater detail, we examined sections
207 from *Trpv1$^{Cre/+}$;R26$^{tdTomato/+}$* kidneys at P1. The tdTomato$^+$ sensory nerves are found
208 adjacent to LRP2$^+$ proximal tubules and E-cadherin (ECAD)$^+$ epithelial structures (**Fig.
209 2B**). Additionally, sensory axons are found adjacent to arteries, arterioles, and glomeruli
210 (**Fig. 2C**). Taken together, these findings show that sensory nerves make up a significant
211 portion of the neuronal network in the developing kidney and associate with kidney
212 structures by early postnatal stages.
213 Nociceptive sensory afferent nerve identity and function can also be defined by the
214 production of neuropeptides such as calcitonin gene-related peptide (CGRP) and
215 substance P. To assess renal peptidergic sensory innervation, we immunostained kidney
216 sections at E14.5, E15.5, E18.5, P0, and adult stages using antibodies for CGRP and
217 substance P. At E14.5 we could not yet detect CGRP$^+$ or substance P$^+$ nerves (**Fig. S3A,**

218 **S3B**). However, by E15.5 we observed CGRP$^+$ sensory nerves that closely associated
219 with renal arteries (**Fig. 3A**). To circumvent cross-reactivity issues due to several of our
220 antibodies being raised in the same species, we crossed the transgenic podocin Cre line
221 (*Pod-Cre^{tg}*) to the *R26^{tdTomato}* reporter (*Pod-Cre$^{tg/+}$;R26$^{tdTomato/tdTomato}$*) thereby labeling all
222 glomerular podocytes with tdTomato. Assessing kidneys from these animals at P0, we
223 found that CGRP$^+$ sensory nerves came in close proximity to glomeruli and proximal
224 tubules (**Fig. 3B**). CGRP$^+$ sensory neurons were also found in adult kidneys, where they
225 similarly associated with the vasculature and Bowman's capsule of glomeruli (**Fig. 3C**).
226 In contrast to CGRP, substance P immunolabelling was not detected until E18.5 where
227 these sensory nerves were observed adjacent to blood vessels and glomeruli (**Fig. 3D**).
228 In the adult kidneys, substance P maintained this localization pattern and these fibers
229 were similarly found associated with the vasculature and Bowman's capsule (**Fig. 3E**).
230 Peripheral neurons innervating the kidney are predominantly unmyelinated C-fibers
231 (Kneupfer and Schramm, 1987; Booth et al., 2015; Osborn et al., 2021). Yet, it has been
232 suggested that some myelinated afferent fibers are present in the kidney (Simon and
233 Schramm, 1983; Kneupfer and Schramm, 1987; Stella and Zanchetti, 1991), although it
234 was unclear if these fibers were peptidergic. To address this, we assessed the
235 colocalization of CGRP+ fibers and Neurofilament heavy polypeptide (NFH), a
236 component of large diameter myelinated axons, in adult kidneys (**Fig. S4**). In the kidney
237 cortex, a few NFH+ fibers were observed although they did not come in proximity to
238 glomeruli and CGRP signal did not overlap with the fibers. In the renal pelvis, we observed
239 minor overlap of NFH$^+$ and CGRP+ along the pelvic urothelium **(Fig. S4)**, supporting the
240 presence, although sparse, of myelinated sensory fibers within the kidney.

241 PIEZO2 is a mechanoreceptor utilized by a subset of peripheral sensory neurons
242 (Coste et al., 2010). PIEZO2$^+$ neurons innervate organs of the urogenital system such as
243 the bladder to help coordinate urination and genital sub-regions to support sexual function
244 (Lam et al., 2023; Marshall et al., 2020). Therefore, we used immunofluorescence staining
245 of PIEZO2 on kidney sections to examine whether PIEZO2$^+$ neurons also innervate the
246 kidney during development. At E15.5, we observed PIEZO2$^+$ neurons associating with
247 CD31$^+$ large vessels (**Fig. 3F**). By P0, we found PIEZO2$^+$ neurons adjacent to glomeruli
248 and proximal tubules (**Fig. 3G**). Collectively, our findings demonstrate the diversity of

249 kidney sensory innervation which consists of both nociceptive and mechanosensitive
250 neurons. The timing of when these neurons and associated neuropeptides can be
251 detected varies throughout kidney development. However, all can be detected by birth
252 and follow a similar pattern of association with the renal vasculature, glomeruli, and
253 tubules.
254
255 ***Retrograde tracing identifies the DRG origin of kidney sensory neurons***
256 The somata of peripheral sensory neurons are located in DRG present along the
257 spinal column. To identify the DRG that contain the sensory neurons projecting to the
258 kidney, we performed retrograde tracing experiments. We injected into the right kidney
259 (ipsilateral) of adult mice the fluorescently labeled neuronal tracer Cholera toxin subunit
260 B (CTB). Four days after the injections, both the injected and non-injected kidney as well
261 as the ipsilateral and contralateral DRG were dissected to determine the origin of kidney
262 sensory innervation (**Fig. 4A**). By examining the fluorescent signal from all cervical,
263 thoracic, lumbar, and sacral DRGs, we determined that kidney sensory innervation traces
264 to the ipsilateral DRG of the lower thoracic (T10-T13), lumbar (L1-L6), and sacral (S1-S2)
265 regions (**Fig. 4B**). However, the majority of sensory innervation projected from the lower
266 thoracic (T10-T13) and upper lumber (L1-L2) regions (**Fig. 4B**). Ipsilateral kidney sections
267 showed CTB^+ nerves near vasculature and glomeruli (**Fig. 4C**). Strikingly, we observed
268 CTB^+ cells within the contralateral DRG of the upper lumbar region (L1-L2), suggesting
269 these DRG may also innervate the kidney (**Fig. 4B**). Additionally, we observed a few
270 CTB^+ nerve fibers around blood vessels in the contralateral kidney (**Fig. 4C**). No
271 difference was identified between male and female mice in the tracing results obtained.
272 Next, we specifically traced $PIEZO2^+$ sensory neurons using the recombinant
273 adeno-associated virus *pAAV-Flex-tdTomato* that we injected into the right kidney of
274 *Piezo2*$^{EGFP\text{-}IRES\text{-}Cre/+}$ mice (**Fig. S5A**). The tracing confirmed innervation of the kidney by
275 $PIEZO2^+$ sensory neurons and shows that the majority of $PIEZO2^+$ nerves project from
276 the lower thoracic (T10-T13) and lumbar (L1 and L2) DRG (**Fig. S5B,C**). Taken together,
277 the retrograde tracing experiments validated sensory innervation of the kidney and
278 uncovered their origins within the lower thoracic, lumbar, and sacral regions (**Fig. 4D,**
279 **S5C**). The observation that CTB^+ cells were found in L1 and L2 contralateral DRG, along

280 with the presence of labeled axons in the contralateral kidney, suggests the possibility of
281 cross communication between the kidneys and DRG on the opposite sides of the body.
282
283 ***Sympathetic and cholinergic innervation of the developing kidney***
284 Sympathetic postganglionic neurons produce tyrosine hydroxylase (TH), an
285 enzyme involved in catecholamine synthesis, and this marker has previously been utilized
286 in the adult kidney to localize sympathetic nerves (Tiniakos et al., 2004; Torres et al.,
287 2021). Thus, to determine the distribution of renal sympathetic nerves in the developing
288 kidney we performed wholemount immunolabeling with a TH antibody at E14.5 and P0
289 (**Fig. 5A,B**). At E14.5, TH^+ nerve fibers were detected in the kidney, overlapping with
290 TUBB3 and tracking with the arteries (**Fig. 5A**). By P0 the sympathetic nerves had
291 branched significantly with the arterial tree and the axons were found navigating around
292 structures such as $LRP2^+$ proximal tubules (**Fig. 5B**). We also examined kidney sections
293 and similarly observed TH^+ axons primarily associated with renal arteries at earlier stages
294 of development (**Fig. 5C**). By P0, the nerves could be found abutting glomeruli and
295 proximal tubules (**Fig. 5D**). We further validated sympathetic nerve identity by co-
296 immunostaining adult kidney sections with the sympathetic marker neuropeptide Y (NPY)
297 and TH. All NPY+ fibers examined, such as those adjacent to glomeruli, were TH+
298 confirming their sympathetic identity (**Fig. 5E**). We also investigated the overlap of TH+
299 and CGRP+ fibers and found them co-associating with glomeruli and in the renal pelvis
300 **(Fig. S6A)**. We then quantified the percent of glomeruli that were innervated by either
301 TH+ fibers, CGRP+ fibers, or both. A previous study performed similar quantitation and
302 found CGRP+ fibers associated with ~48% of glomeruli in wild type adult mice (Tyshynsky
303 et al., 2023). Corroborating these findings, our analyses identified 40% of glomeruli were
304 associated with CGRP+ fibers. TH+ axons associated with 50% of glomeruli and ~37%
305 were innervated by both CGRP+ and TH+ axons. **(Fig. S6B)**. Taken together, these
306 findings show that sympathetic neurons innervate the kidney early in development,
307 tracking with the vasculature and colocalizing with CGRP+ fibers as they make their way
308 to nephron targets such as tubules and glomeruli in alignment with their known
309 physiological functions (DiBona, 2004; DiBona & Kopp, 1997; Osborn & Foss, 2017; Sata
310 et al., 2018).

311 Previous studies showed that during development, TH may also be produced by
312 cholinergic parasympathetic nerves (Howard, 2005). A recent study demonstrated
313 parasympathetic innervation of the main renal artery and pelvis, yet there remains no
314 anatomic evidence of significant parasympathetic innervation into the kidney. To identify
315 whether there are cholinergic nerves in the developing kidney, we immunostained
316 sections at E14.5, E15.5, P0, and adult for the cholinergic marker vesicular acetylcholine
317 transporter (VAChT) (**Fig. S7**). We did not observe VAChT$^+$ nerves overlapping with pan-
318 neuronal marker TUBB3 at E14.5 (**Fig. S7A**) even though the first nerve fibers innervating
319 the kidney at E14.5 were TH$^+$ (**Fig. 5A**). By E15.5, we observed that TUBB3$^+$ nerves
320 overlapped with VAChT signal, and these nerves were primarily associated with the renal
321 artery in the kidney shown by CD31 immunostaining (**Fig. S7B**). Vascular-associated
322 innervation increased by E16.5, and we observed VAChT$^+$ fibers around proximal tubules
323 and glomeruli at P0 (**Fig. S7C**). In adults, the VAChT$^+$ fibers were found associated with
324 the kidney vasculature (**Fig. S7D**). In sum, these data lend support to the presence of
325 parasympathetic innervation into the kidney with axons reaching nephrons.
326
327 ***Evidence for the establishment of neuroeffector junctions during kidney***
328 ***development***
329 In order to exert an impact on kidney development and physiology, neurons need
330 to establish functional crosstalk with kidney cells. To investigate the formation of
331 neuroeffector junctions, synapse-like structures that form between neurons and non-
332 neuronal cells, we characterized the cellular localization of a synaptic marker by
333 immunofluorescence on cryosectioned kidneys. Using an antibody raised against
334 synapsin I (SYN1), a membrane-associated phosphoprotein contained within small
335 synaptic vesicles of presynaptic nerves, we investigated if and at which stage SYN1 is
336 detected. At E14.5 SYN1$^+$ axons were observed around the vasculature (**Fig. 6A**). At
337 E16.5, there was similar localization of SYN1$^+$ nerves mainly associated with the
338 vasculature (**Fig. 6A**). By P0, SYN1$^+$ axons were localized near proximal tubules and
339 glomeruli (**Fig. 6B**). A similar pattern was retained in the adult with SYN1$^+$ axons found
340 along the vasculature and adjacent to glomeruli (**Fig. 6C**).

341 Next, we investigated the developmental expression of receptors associated with
342 various neuronal signaling mechanisms and known post-synaptic markers to understand
343 which kidney cells are responsive to neuronal signaling. We utilized a publicly available
344 single cell RNA-seq dataset from the E18.5 kidney to obtain the enrichment of these
345 factors in the various cells of the developing kidney (Combes et al., 2019) (**Fig. S8**). These
346 data show that a variety of cell types and structures including nephron progenitors,
347 stromal cells, renal vesicles, and the S-shaped body express α-adrenergic receptors
348 *Adra1a* and *Adra1b*, whereas *Adra2a* and *Adra2b* were enriched in the distal tubules,
349 ureteric epithelium, and proximal tubules (**Fig. S8A**). We also noted the β-adrenergic
350 receptor *Adrb2* was strongly enriched in the resident immune cells while *Adrb3* was
351 expressed by stromal cells (**Fig. S8A**). Next, we also looked for the expression of major
352 purinergic receptors in the developing kidney. Many of the ATP and Adenosine receptors
353 including *P2rx4, P2rx7, P2ry6, P2yr12, P2yr13, P2yr14, Lpar6,* and *Lpar4* showed
354 enrichment in the resident immune cells. Endothelial cells, tubule epithelium, and ureteric
355 epithelium showed expression of *Ador2a, P2ry1, Lpar6, Lpar4,* and *Adora1* while *P2rx4*
356 and *P2ry14* were moderately enriched in podocytes (**Fig. S8B**). Lastly, we observed the
357 enrichment of known post-synaptic markers or synapse-promoting markers like *Vamp2,*
358 *Tenm3, Tenm4, Ephb1, Ephb3, Epha2, and Grm7* by podocytes, *Nlgn1, Epha2, Ephb1,*
359 *and Ephb4* by endothelial cells, and *Gria3, Ephb2, Ephb3, Ephb4, Ephb6, Epha1, Epha4,*
360 *Epha7, Tenm2, Dlg4, Dlg1, Nlgn3* by the distal and proximal tubules (**Fig. S8C**).
361 Collectively, the single-cell expression data provides evidence that cells within the
362 developing kidney express a variety of receptors and post-synaptic markers suggesting
363 they are competent to receive and respond to neuronal-derived signals.
364
365 ***The spatial organization of nerves is conserved in the adult human kidney***
366 Given the specific distribution of kidney nerves around important structures such
367 as glomeruli and tubules in the mouse, we aimed to validate that innervation of structures
368 in the human adult kidney was similar. First, we immunostained adult human cortex
369 cryosections with sympathetic nerve marker TH. We observed TH^+ axons looping around
370 glomeruli and associating with the Bowman's capsule similar to the mouse. These
371 sympathetic nerves were also found near epithelial structures (ECAD+) (**Fig. 7A; Movie**

372 **S6**). Next, we sought to confirm the presence of PIEZO2$^+$ mechanosensory afferents in
373 the adult human kidney. We identified PIEZO2$^+$ nerves that were closely associated with
374 glomeruli and vessels as well as the kidney epithelium (**Fig. 7B**). To validate that the
375 nerves were actively signaling we assayed for the presence of neuroeffector junctions by
376 immunostaining for SYN1. We observed SYN1$^+$ nerve fibers looping around glomeruli
377 and around tubules (**Fig. 7C, Movie S7**). Taken together, these data show that the close
378 association of both sympathetic and sensory nerves with vessels and nephrons is
379 conserved in humans.
380

381 **Discussion**

382 In this study, we set out to investigate the process of kidney innervation across
383 embryonic and postnatal mouse development. We generated spatiotemporal maps of
384 innervation using markers specific to various classes of axons and identified the presence
385 of both sensory and sympathetic nerves, as well as evidence for parasympathetic
386 innervation. High resolution imaging of kidney sections provided insights into the
387 association of nerves with kidney structures such as the vasculature, glomeruli, and
388 tubules and the possible establishment of neuroeffector junctions. Finally, we validated
389 that the human kidney shows similar associations of sympathetic and sensory nerve
390 subclasses with nephron structures. Altogether, we have garnered substantial new
391 insights into the process of kidney innervation with implications for both development and
392 physiological regulation.
393

394 ***The close association of nerves with kidney vasculature***

395 We established that kidney innervation begins at E13.5 and coincides with the
396 initiation of arterial differentiation as vascular smooth muscle cells associate with the
397 nascent endothelium. In the developing kidney, it has been shown that arterial
398 differentiation is first established at E13.5 and progresses toward the kidney periphery
399 (Daniel et al., 2018; Luo et al., 2023). Our findings of a strict association of axons with
400 vascular smooth muscle cells correlates with a recent description of kidney innervation
401 as well as our own recent studies (Honeycutt et al., 2023; Tarnick et al., 2023). We
402 hypothesize that SMA+ vascular mural cells may be signaling to the axons, thereby

403 guiding the nerves as the arteries differentiate and grow. This has been shown in other
404 systems with axons responding to vascular-derived cues like artemin (*Artn1*) and
405 neurotrophin 3 (*Ntf3*) (Glebova & Ginty, 2005). In the kidney, *Ntf3* is expressed by
406 nephron progenitor cells and early developing nephrons whereas *Artn1* does not appear
407 to be expressed, as inferred from single cell RNA-seq data of the developing (E18.5)
408 kidney (Combes et al., 2019). Whether *Ntf3* or *Artn1* are expressed by the vasculature at
409 earlier stages and mediate kidney innervation not been investigated to date. Once
410 established, continued axonal growth and survival relies on neurotrophic factors such as
411 nerve growth factor (NGF). During nephrogenesis, NGF is produced by cortical,
412 medullary, and ureteric stroma (Combes et al., 2019; Glebova & Ginty, 2004).
413 Additionally, it was established that NGF is required for the complete sympathetic
414 innervation of the kidney via its interaction with its innate receptor tropomyosin receptor
415 kinase A (TRKA) (Glebova & Ginty, 2004). Moreover, proper innervation also requires
416 chemotactic guidance cues released by adjacent cells within the tissue. In the kidney, we
417 and others have established that proper patterning of the neurovascular network is
418 mediated by the guidance cue netrin-1 (Honeycutt et al., 2023; Luo et al., 2023). However,
419 we established that the endothelium is the primary responder to netrin-1 guidance cues,
420 with the nerves following the vascular pattern, suggesting the SMA$^+$ vascular mural cells
421 themselves play a significant role in guiding kidney innervation (Honeycutt et al., 2023).
422 While it has been established that netrin-1 plays a key role in synapse formation and
423 axonal regeneration in the brain, we do not know whether the same is true in the kidney
424 (Zheng et al., 2018). Additional studies are necessary to establish the full complement of
425 cues necessary for proper kidney innervation and the establishment of functional
426 crosstalk.
427
428 ***The diversity of kidney nerves***
429 During kidney development, we found that both sensory and sympathetic nerves
430 innervate the tissue early in development and branch following the arterial tree. Sensory
431 nerves could be classified as nociceptive by TRPV1$^+$ lineage tracing. The limitation of this
432 approach is that as neurons mature, they may not remain TRPV1$^+$. As such, and with the
433 lack of our ability to identify a TRPV1 antibody that worked on our kidneys, this lineage

434 trace only serves as a proxy for TRPV1$^+$ nerves that innervate the kidney from the onset.
435 However, we were able to further classify the sensory neurons by their production of the
436 neuropeptides CGRP and substance P. CGRP$^+$ nerves were identified earlier in
437 development than substance P$^+$ nerves (E15.5 vs. E18.5), but both did not appear until
438 innervation had already been established for several days. With the importance of
439 neurotrophic factors for proper sensory afferent nerve function, these delays in production
440 could be due to changes in molecular cues required for their specific growth and function
441 (Ernsberger et al., 2020; Golden et al., 2010). The expression of their innate target
442 receptor on kidney cells could also play an important role in triggering neuropeptide
443 production. Despite these differences, all the sensory nerve markers showed similar
444 tracking with the vasculature and association with kidney target structures such as
445 glomeruli and tubules around E18.5 to P0.

446 Recent studies have established the expression of the *Piezo2* mechanosensory
447 receptor by stromal progenitor cells during kidney development, as well as
448 juxtaglomerular (JG) cells and glomerular mesangial cells in the adult kidney (Mochida et
449 al., 2022, Hill et al., 2023). While our antibody labeling did not detect these PIEZO2$^+$ cells,
450 this was also noted in the study by Mochida et al. where RNAScope *in situ* hybridization
451 was necessary to detect *Piezo2* expression. We have established the presence of
452 PIEZO2$^+$ sensory nerves in both the mouse and human kidney where they associate with
453 the vasculature, glomeruli, and proximal tubules. We hypothesize that these sensory
454 axons are poised to sense changes in pressure or volume within the kidney. It has been
455 established that PIEZO2$^+$ cells in the bladder communicate with pressure sensitive
456 PIEZO2$^+$ afferent nerves to mediate micturition (Marshall et al., 2020), and PIEZO2
457 signaling is critical for sexual function (Lam et al., 2023). We recently reported that
458 PIEZO2 in JG cells modulates renin levels (Hill et al., 2023). However, further
459 investigation is required to understand whether such communication between PIEZO2$^+$
460 kidney cells and PIEZO2$^+$ sensory neurons play a role in development or physiological
461 function. Interestingly, many of these sensory nerves are seen looping in a “hairpin”
462 fashion around glomeruli and tubules. Such anatomic position may better enable the
463 ability to sense changes in pressure, volume, filtration rate, and tubule physiology
464 ensuring homeostatic control. The looping may also enable innervation of structures

465 within the kidney without the need for a singular synapse to each kidney cell. These
466 findings further emphasize the need for studies investigating the physiological role of
467 sensory afferent nerves in the control of kidney development and function in health and
468 disease.

469 In addition to the sensory nerves, we also showed that TH^+ sympathetic efferent
470 nerves innervate the developing kidney. TH^+ axons were detected as early as E14.5 and
471 as development progressed, TH^+ nerves associated with the vasculature, tubules, and
472 glomeruli. Association with these structures correlates with the known physiological
473 functions of sympathetic nerves in modulating vascular tone, tubular sodium reabsorption,
474 and renin release by JG cells (Osborn et al., 2021; Osborn & Foss, 2017). It has been
475 established that renal sympathetic nerves contribute to the pathogenesis of hypertension.
476 Thus, procedures like catheter-based renal denervation are seen as novel therapies that
477 could reduce blood pressure in hypertensive patients (Esler et al., 2012; Krum et al., 2013,
478 2014). However, this procedure non-selectively targets all renal nerves and with our
479 observation of the significant overlap of sensory and sympathetic fibers innervating
480 glomeruli, a deeper understanding of the interplay between sympathetic and sensory
481 nerves in the mediation of physiology may inform efforts to optimize these ablation
482 strategies.

483 Most visceral organs are innervated by both sympathetic and parasympathetic
484 nerves. This is no exception to the kidney which was first hypothesized to harbor
485 parasympathetic nerves that enter the kidney along the renal vasculature (Furness, 1999;
486 Mitchell, 1950). Yet, there remains no significant anatomic evidence of extensive
487 parasympathetic innervation within the kidney, and this remains a topic of debate. In our
488 study, we observed $TUBB3^+$ nerve fibers which colocalized with the cholinergic marker
489 VAChT. However, this could represent a subset of immature sympathetic nerves
490 expressing both VAChT and TH, although as development progressed, we observed
491 $VAChT^+$ nerves in the cortex associating with structures such as tubules which are more
492 likely to represent mature, functional parasympathetic nerves. Higher resolution imaging
493 studies are needed to determine if these are sympathetic nerves expressing cholinergic
494 markers or whether they represent separate classes. Recently, research by Cheng et al.
495 on adult mouse renal arteries showed the presence of periarterial cholinergic nerves

496 which were separate from sympathetic and sensory nerve fibers (Cheng et al., 2022).
497 Together, these findings point to the potential for greater contribution of parasympathetic
498 activity in the modulation or kidney function than has been previously appreciated,
499 although further characterization is necessary.
500
501 ***Common DRG projections to organs of the urogenital system***
502 The regulation of kidney homeostasis is in part maintained by neuronal modulation.
503 Ablation of renal nerve activity is widely seen as a way to treat diseases like hypertension.
504 Accurate mapping and understanding the molecular identity of kidney nerves will help
505 guide such interventions. However, studies have largely focused on kidney sympathetic
506 nerves and only recently has the contribution of sensory neurons to physiological
507 regulation been more thoroughly investigated (Banek et al., 2016; Ong et al., 2019;
508 Osborn et al., 2021). Building on these previous studies, we found that kidney sensory
509 innervation is substantial and molecularly diverse. Axons from sensory neurons form an
510 extensive network in the developing kidney that continues to expand with maturation.
511 Validation of sensory innervation was provided by retrograde tracing and identified the
512 DRG origins of these nerves. Kidney sensory innervation traces to the lower thoracic
513 region from DRG T10-T13, the lumbar region from DRG L1-L6, and the sacral region from
514 DRG S1 and S2. We cannot absolutely rule out some leakage of tracer into the pelvis
515 and ureter, thus expanding the labeling to lower lumbar and sacral DRG, albeit at weaker
516 levels. Despite this variable DRG labeling, the majority of axons innervating the kidney
517 project from T10-13 and L1-L2. PIEZO2^{+} neurons similarly traced to the DRG at these
518 levels. Tracing performed in the mouse bladder and prostate via the application of
519 FastBlue dye revealed similar projection of neurons from T13, L1, L2, L6, and S1 (Lee
520 et al., 2016). This suggests that organs of the genitourinary system are largely innervated
521 from common DRG. Interestingly, our CTB tracing experiment also showed that
522 contralateral DRG at L1 and L2 were positive for CTB. These data suggest that some
523 axons innervating the kidney might originate from contralateral DRG or that the same
524 DRG in the ipsilateral side sends axons to both kidneys. Concurrent retrograde labeling
525 of sensory nerves in the bladder and colon showed that dichotomizing afferent nerves
526 coming from an individual DRG neuron innervate both the colon and the bladder

527 (Christianson et al., 2007). Such connectivity is important for integrating sensory input
528 from multiple organs and likely plays a major role in conditions such as pelvic pain
529 disorders.
530
531 ***Establishing crosstalk during kidney development***
532 During development the nerves lie in close association with the vasculature,
533 tubules, and glomeruli suggesting potential functional crosstalk. Sympathetic and sensory
534 nerves branch with the vasculature and dissociate to navigate through the tissue where
535 they appear to loop around glomeruli and lie adjacent to tubules. Such close association
536 likely allows for the formation of neuroeffector junctions with target structures and nerves
537 to functionally innervate multiple structures as axons navigate around them. As reviewed
538 previously (Barajas et al., 1984; DiBona & Kopp, 1997; Osborn et al., 2021), these fiber
539 varicosities could impact adjacent kidney cells by establishing neuroeffector junctions
540 more than 50μm away from the neurotransmitter release site, allowing for diffusion
541 throughout the interstitium and to target cells. To investigate the presence of
542 neuroeffector junctions in the kidney, we assessed the localization of synapsin I, which is
543 a major component of pre-synaptic vesicles and important for axonogenesis (Chin et al.,
544 1995). Early during development, we observed that synapsin I is mainly localized near
545 vasculature and this localization profile is extended to the glomeruli and tubules by E18.5.
546 Such findings agree with our current understanding of kidney development and
547 physiology. Mouse kidney development continues postnatally contrary to human kidney
548 development which is finished before birth (McMahon, 2016). We also know that the
549 mouse kidney forms around 90% of its nephrons towards the end of ureteric branching
550 with 40% of them differentiating after birth (Smyth, 2021). Yet, kidney function must be
551 established very early on in newborn pups. Thus, it is likely important to establish proper
552 innervation of the developing kidney to regulate homeostasis. Interestingly, data mining
553 through publicly available single cell RNA-seq datasets of E18.5 kidneys (Combes et al.,
554 2019) suggests that many AMPA (*Gria1*, *Gria3*, *Gria4*) and NMDA (*Grin3a*) receptors are
555 expressed by different nephron and stromal progenitors, as well as early proximal tubules.
556 While it has been established that glutamatergic signaling via NMDA maintains the
557 epithelial phenotype of proximal tubular cells through calcium signaling in a proximal

558 tubule cell line (HK-2) (Bozic et al., 2011), it remains unclear what role glutamate transport
559 may play in the proper development of proximal tubules. Overall, the expression of
560 neurotransmitter receptors and postsynaptic markers in the developing kidney suggests
561 the potential for several neuronal signaling mechanisms that regulate development and
562 function.
563
564 ***Limitations of our studies***
565 To our knowledge, our study is the first to provide a thorough characterization of
566 kidney innervation detailing the spatial and temporal establishment of nerve networks
567 during development, including association and putative crosstalk with target structures.
568 Importantly, we establish that a significant portion of the nerve network consists of
569 sensory afferent axons with the novel identification of PIEZO2^{+} mechanosensory
570 neurons. However, it is important to note some assumptions which guided our study. For
571 the classification of noradrenergic sympathetic nerves, we use TH as a marker. The
572 strong expression of TH by sympathetic ganglion near the descending aorta support our
573 finding that TH^{+} sympathetic nerves are abundant in the developing kidney. However,
574 some TH^{+} axons in the developing kidney may project from the DRG (Meerschaert et al.,
575 2020) thus we cannot omit that a certain percentage of these nerves may be sensory,
576 although this is likely to be a minor percentage given the low level of TH expression within
577 sensory ganglia prior to birth (Smith-Anttila et al., 2021). Additionally, the colocalization
578 of TH and NPY in adults suggests that any significant sensory nerve production of TH is
579 resolved by this point. Finally, we relied on the careful study of technical and biological
580 replicates but did not quantify axon metrics such as density or percent of sympathetic
581 versus sensory nerves aside from our adult glomerular quantitation. Hence, there is a
582 possibility that we did not identify more subtle differences among stages and classes of
583 nerves, in addition to sex differences. Future investigations are necessary to parse out
584 these details and to also determine the significance of these nerves to overall kidney
585 development and the establishment of proper function.
586
587 **<u>Materials and methods</u>**
588 ***Animals***

589 All procedures and experiments were performed according to the guidelines of the
590 National Institutes of Health Guide for the Care and Use of Laboratory Animals and were
591 approved by the Institutional Animal Care and Use Committees of The University of North
592 Carolina at Chapel Hill (protocols 19-183 and 22-136) and performed under the policies
593 and recommendations of the International Association for the Study of Pain and approved
594 by the Scripps Research Animal Care and Use Committee (protocol 08-0136). Mice were
595 kept in standard housing with a 12-h light–dark cycle, with the room temperature kept
596 around 22 °C, and humidity between 30% and 80% (not controlled). Mice were kept on
597 pelleted paper (Scripps) or corncob (UNC) bedding and provided with paper square
598 nestlets and polyvinyl chloride pipe (Scripps) or hut (UNC) enrichment with ad libitum
599 access to food and water. Adult Swiss Webster (Taconic stock: SW MPF) and C57Bl6/J
600 (Jackson Labs (JAX) stock #: 000664) mice were purchased from the respective vendor
601 for experiments and in house matings. Swiss Webster incrosses were utilized for all
602 experiments involving only embryonic and postnatal wild type mice. C57Bl/6J mice were
603 utilized for maintenance of transgenic and knock-in lines and adult analyses. Mice utilized
604 for adult analyses were 8 weeks to 4 months of age. *Trpv1*^{Cre} (JAX stock
605 #:017769)(Cavanaugh et al., 2011) were maintained as a homozygous line, *Pod-Cre*^{tg}
606 mice (JAX stock #:008205)(Moeller et al., 2003) were maintained as heterozygotes,
607 *R26*^{tdTomato} (JAX stock #:007914)(Madisen et al., 2010) mice were maintained as a
608 homozygous line, and *Piezo2*$^{EGFP\text{-}IRES\text{-}Cre}$ (JAX stock #:027719) (Woo et al., 2014) mice
609 were maintained as heterozygotes.
610
611 ***Tissue collection and processing***
612 For all mouse experiments, matings were set up in the afternoon and copulation
613 plugs found the following day were designated as embryonic day (E)0.5. The day of birth
614 was considered postnatal day (P)0. This occurred at E19.5, births earlier or later than
615 E19.5 were not utilized in these studies. At the desired developmental time point,
616 pregnant dams were sacrificed by CO_2 inhalation, and death was confirmed by cervical
617 dislocation. Mouse embryos were excised from the uterus and kidneys or whole
618 urogenital systems dissected in ice-cold 1x phosphate-buffered saline (PBS). For genetic
619 crosses, tail or ear clips were taken and incubated with DirectPCR lysis buffer (Viagen

620 Biotech, 102-T) containing 10μg/mL proteinase K (Sigma, 3115836001), incubated at
621 55°C overnight, and denatured at 95°C for 20 min the next day. Genotyping was
622 performed using JAX genotyping protocols and recommended primers with the following
623 PCR parameters: annealing temperature T_{anl} = 58°C, elongation time t_{elg} = 40 sec for 35
624 cycles. To ensure biological significance, we analyzed a minimum of 3 animals per
625 neuronal marker for both sexes at the following stages: E12.5, E13.5, E14.5, E16.5,
626 E18.5, P0, P7, and adults (6-10 weeks old). For tissue processing, all steps below were
627 performed on rotating shakers. Harvested kidneys or urogenital systems from embryonic
628 and postnatal mice were fixed by immersion in fresh ice-cold 4% PFA-PBS (Fishersci,
629 15714) at 4°C for 30 min, while kidneys obtained from juvenile and adult mice were fixed
630 by immersion in fresh ice-cold 4% PFA-PBS at 4°C for 2 hours. Next, all kidneys were
631 washed in ice-cold 1x PBS three times for 10 min each at room temperature and stored
632 at 4°C in 1x PBS until use. All kidneys destined to be sectioned were incubated in 30%
633 sucrose-PBS solution at 4°C overnight. The next day, kidneys were then embedded in
634 Tissue freezing media (Fishersci, 23730571) and sectioned at 12μm on a Leica cryostat
635 CM1850. Slides were stored at -80°C until use.
636 Human kidney tissue samples were obtained from the UNC Tissue Procurement
637 Facility and were de-identified and therefore were exempt from IRB approval. Tissue was
638 obtained as a frozen block. A small piece of tissue was removed with a razor blade, fixed
639 for 10 min in 4% paraformaldehyde, and subsequent processing for cryosectioning and
640 immunofluorescence was carried out as for the mouse.
641
642 ***Cholera Toxin B(CTB) and pAAV-FLEX-tdTomato retrograde tracing***
643 Surgeries were performed as in Woodard et al., 2018. Briefly, mice were
644 anesthetized with isoflurane inhalation and surgery started after all-paw reflexes
645 disappeared. The right kidney was accessed via flank incision after the animal was
646 shaved from shoulder to rump and flank to spine with a shaver designed for pet grooming.
647 After appropriate cleaning of the surgical site, the skin was pinched with tweezers and a
648 cut of approximately 1cm from the spine and below the ribcage was made with scissors.
649 A similar cut was made on the muscle layer underneath the skin, the kidney was exposed
650 and carefully isolated with cotton-tip applicators from peripheral fat or connective tissues

651 in order to not disrupt nerve connections. Injections were made with a 10ul Hamilton
652 syringe attached to a 32G needle. Tracers were injected at an approximate rate of
653 1µl/30sec and the needle was left inside the tissue after injection for an additional 1
654 minute to avoid back-leak. For retrograde labeling of the DRG innervating the kidney, 4
655 injections of 3µl 0.2% CTB-555 (Invitrogen, C34776) were administered to 4 males and 4
656 females on a C57Bl6/J and Swiss Webster background. For retrograde labeling of the
657 PIEZO2^{+} nerves innervating the kidney, 4 injections of 5µl of AAV PHP.S (Addgene,
658 28306-PHP.S, *pAAV-FLEX-tdTomato*; deposited by Viviana Gradinaru, Chan et al. 2017)
659 were administered to 2 males and 2 females which were *Piezo2*$^{EGFP\text{-}IRES\text{-}Cre/+}$. All injections
660 were administered directly into kidney tissue through the renal capsule. The 4 injections
661 consisted of one cortical injection per pole of the kidney, one injection in the medulla, and
662 one injection in the renal pelvis. After injections, the muscle and skin were closed with
663 sutures, and bupivacaine was administered for analgesia. After suturing, mice were
664 housed in a clean cage with heat pads underneath until ambulatory. Mice were
665 euthanized 4 days after CTB injections and 4 weeks after AAV PHP.S injections. Mice
666 were perfused with 30ml 1x PBS and 20ml 4% PFA-PBS with kidneys and DRG collected
667 for tissue sectioning and imaging.
668
669 ***Section immunofluorescence***
670 Kidney sections for immunofluorescence were removed from the -80°C freezer and
671 allowed to equilibrate to room temperature for 10 min. Sections were rehydrated, and the
672 freezing medium was removed by incubating the slide in 1x PBS for 10 min in a Coplin
673 jar. After rehydration, excess PBS was removed from the slide then a hydrophobic barrier
674 was drawn around the section using a hydrophobic pap pen (Vector Laboratories, Cat#H-
675 4000). Sections were incubated for 30 min in blocking solution (ice-cold PBS solution with
676 4% donkey serum (Equitech-Bio, SD30-0100), 1% bovine serum albumin (Fishersci,
677 BP9706-100), and 0.25% Triton X-100 (Fishersci, BP151-500). Slides were then
678 incubated at room temperature for 2 hours covered from light with primary antibodies in
679 block solution (see Supplemental Table 1 for primary antibodies utilized; PIEZO2
680 antibodies were combined as a mixture for optimal detection although each work
681 independently as validated by co-immunostaining with GFP on DRG isolated from

682 *Piezo2*$^{EGFP\text{-}IRES\text{-}Cre/+}$ mice). After primary incubation, slides were washed 3 times for 5 min
683 at room temperature covered from light with wash solution (PBS + 0.25% Triton X-100)
684 before incubating them for 45 min at room temperature covered from light with the
685 appropriate Alexa Fluor secondary antibody (Life Technologies, 488, 568, or 647
686 conjugated; 1:1000) in blocking solution. Finally, slides were washed 4 times for 5min at
687 room temperature covered from light using wash solution with the last wash containing
688 DAPI diluted at 1:10000. Slides were mounted using Prolong gold mounting media
689 (ThermoFisher, P36930), and images were captured with a Zeiss 880 confocal laser
690 scanning microscope.

691 For the NFH, NPY/TH and CGRP/TH immunofluorescence, C57BL6/J adult mice
692 were euthanized via isoflurane overdose and transcardially perfused with 20 mL ice-cold
693 PBS pH 7.4 followed by 30 mL ice-cold 4% PFA in PBS. Kidneys were dissected and
694 fixed overnight in 4% PFA at 4ºC. Kidneys were then rinsed in PBS and cryoprotected in
695 30% sucrose for 24-48 hours at 4ºC prior to embedding and freezing in OCT medium
696 (Sakura). 20 µm sections were prepared on glass slides using a cryostat. Tissues were
697 allowed to air-dry for 30 minutes at room temperature and hydrophobic barriers were
698 drawn using a PAP pen (Vector Biolabs, H-4000). Slides were washed in PBS and
699 blocked in 5% Normal Donkey Serum (for NPY IHC, Sigma-Aldrich, D9663) or Normal
700 Goat Serum (all other experiments, Life Technologies, PCN5000) in PBS with 0.3% Triton
701 X-100 (PBST) for two hours at room temperature in a humidified chamber. Slides were
702 incubated overnight at 4ºC in the following primary antibodies in 0.1% PBST: CGRP, TH
703 (chicken), NFH, or NPY. Slides were washed in 0.3% PBST followed by PBS and then
704 incubated for two hours at room temperature in the following secondary antibodies in
705 0.1% PBST: donkey anti-goat 647 (Life Technologies, A21447, 1:1000), donkey anti-
706 chicken 488 (Life Technologies, A78948, 1:1000), goat anti-Rabbit 647 (Life
707 Technologies, A21245, 1:1000), goat anti-chicken 488 (Life Technologies, A11039,
708 1:1000). Donkey secondary antibodies were used for NPY staining experiments and goat
709 secondary antibodies were used for all other experiments. Samples were mounted using
710 Fluoromount G + DAPI (Life Technologies, 00-4959-52) and sealed with No. 1.5
711 coverslips and clear nail polish and stored at 4ºC. Samples were imaged on a Nikon AX
712 confocal microscope.

713

714 ***CGRP/TH glomeruli quantification***

715 Maximum intensity z-projections were generated and glomeruli were identified
716 from the DAPI signal as regions of interest (ROI). Each individual ROI was manually
717 assessed for the presence of TH or CGRP immunoreactivity at the Bowman's capsule or
718 at the juxtaglomerular region adjoining the glomerulus and the arterioles. ROI with
719 immunoreactivity at either location were determined to be innervated. For the TH staining,
720 substantial non-neuronal tubular immunoreactivity was observed that was readily
721 distinguishable from nerve fibers. The tubular immunoreactivity was not used to quantify
722 innervation. FIJI (2.0.0) and Prism 10 (10.1.1) software were utilized for analyses.

723

724 ***Wholemount immunofluorescence and tissue clearing***

725 For mouse embryonic and postnatal kidneys or urogenital systems (E12.5-P7), we
726 used a modified version of the original iDISCO protocol (Renier et al., 2014) for
727 wholemount immunolabelling (see Supplemental Table 2) using validated antibodies and
728 concentrations indicated in Supplemental Table 1. All steps are performed on rotating
729 shakers. We first incubated whole pre-fixed tissue in 1ml blocking solution (ice-cold PBS
730 solution with 10% (v/v) Heat Inactivated Sheep Serum (HISS) (ThermoFisher, 16070096)
731 and 0.5% (v/v) Triton X-100) for 1hr at room temperature. Then, we incubated the blocked
732 kidney in 1ml primary antibody in block solution for 7 days at 4°C while covered from light.
733 The labeled kidney was then washed using 1ml wash buffer (PBS solution with 0.25%
734 Triton X-100) for a whole day at room temperature covered from light with wash solution
735 changed every 1 hour. After washing, labeled kidneys were incubated in 1ml secondary
736 antibody in block solution at a concentration of 1:1000 for 3.5 days at 4°C while covered
737 from light. After secondary antibody labeling, kidneys were washed again using 1ml wash
738 buffer for a whole day at room temperature covered from light with wash solution changed
739 every 1 hour. Before optical clearing, successful labeling was checked on a widefield
740 Leica fluorescent microscope (Leica DMi8). Labeled kidneys were then embedded in 1%
741 agarose (Fishersci, BP160-500) gel made with 1x TAE, the agarose block was cut to a
742 size of 5mmx5mm to ensure proper mounting on the light-sheet microscope. To clear
743 kidneys, we first dehydrated the agarose block in a methanol-H_20 (Fishersci, A433P-4)

series wash at room temperature (25%, 50%, 75%, and 100%) for 1 hour each minimum covered from light. Next, dehydrated agarose blocks were incubated in 66% v/v dichloromethane (DCM) (Sigma, 270997-2L)/33% v/v methanol for 3 hours at room temperature covered from light. Following this, the agarose blocks were then incubated in 100% DCM for 15min x 2 at room temperature covered from light. Finally, the fully dehydrated agarose blocks were incubated in 100% v/v dibenzyl ether (DBE) (Sigma, 33630-1L) and stored at room temperature away from light. The blocks became transparent and invisible within 5-7hr and were stored in DBE until imaging. The DBE was changed out for fresh DBE before imaging the sample.

3D light-sheet and confocal imaging

All whole-mount images were obtained using the LaVision BioTec Ultramicroscope II light-sheet system at the UNC Microscopy Services Laboratory (MSL). This light-sheet is outfitted with an Andor Zyla 5.5 sCMOS detector, an Olympus MVPLAPO 2X/0.5 objective coupled to a zoom body ranging from 1.26x to 12.6x with a corrected dipping cap and a working distance of 5.7mm. All whole-mount images in this study were imaged with laser wavelengths: 488, 561, and 647nm as well as 3 angled light-sheet from one side only with the following parameters: sheet NA of 0.016, horizontal focus set in the middle of the sample, correction collar set at 3.5 and 2µm Z-spacing (step size). All tiff images are generated in 16-bit. All confocal images were obtained using a Zeiss 880 confocal laser scanning microscope in the UNC Hooker Imaging Core via the Zen 2 software with 34-channel gallium arsenide phosphide (GaAsP) detectors. All images obtained were imaged using a Plan-Neofluar 40x/NA:1.3 or 63x/NA:1.4 oil objective with the following working distance respectively: 0.21mm and 0.19mm. Pinhole size of 1AU set on the longest wavelength fluorophore with the same diameter size for all the rest. All image acquisition settings can be found in Supplemental Table 3.

Image processing

Images, 3D volume, and movies were generated using Imaris x64 software version 9.9.1. All stack images obtained from light-sheet imaging were first converted into an imaris file (.ims) using Imaris File Converter version 9.8.2. All wholemount images and

775 videos were obtained using the “snapshot” and “animation” tools in Imaris 9.9.1. files
776 obtained from Zeiss confocal microscope (.czi) were converted into an Imaris file using
777 Imaris File Converter 9.8.2. Tilescan images were stitched with 20% overlapped using
778 Imaris stitcher 9.9.1 and image analysis was done in Imaris version 9.9.1.
779
780 ***Receptor and postsynaptic marker scRNA-seq enrichment***
781 To identify the kidney cell populations in which nerve associated receptors and
782 markers were expressed, the selected genes were analyzed for their relative enrichment
783 within the single cell RNA-seq data from E18.5 kidneys (Combes et al., 2019). Heatmaps
784 were generated in R (R Core Team, 2021) using the ggplot2 package (Wickham, 2009)
785 and ComplexHeatmap (Gu et al. 2016). Log fold change values were obtained from
786 Combes et al., 2019 Table S1 "lookup" tab.
787
788 **Acknowledgments**
789 We thank members of the O’Brien Lab for their critical insights throughout the
790 project. We would like to thank Dr. Pablo Ariel director of the UNC Microscopy Services
791 Laboratory for expert training in light-sheet image acquisition and analysis and lending
792 his expertise throughout the project, and Dr. Wendy Salmon director of the UNC Hooker
793 Imaging Core for confocal microscopy imaging training. The Microscopy Services
794 Laboratory in the Department of Pathology and Laboratory Medicine and the Department
795 of Cell Biology and Physiology Hooker Imaging Core are supported by the NIH
796 P30CA016086 Cancer Center Core Support Grant to the UNC Lineberger
797 Comprehensive Cancer Center. Light-sheet microscopy at MSL is also supported in part
798 by the North Carolina Biotech Center Institutional Support Grant 2016-IDG-1016, and
799 Andor Dragonfly microscope was funded with support from National Institutes of Health
800 grant S10OD030223.
801
802 **Conflict of Interest**
803 The authors declare that they have no conflict of interest
804
805 **Funding**

This work was supported by AHA Predoctoral Fellowship 24PRE1241584 to P-E.Y.N., NIH R01DK121014 to L.L.O, NIH R01DA044481 and W81XWH-15-1-0076 Neurosensory Research Award from the Department of Defense to G.S., NINDS 1K99NS133478 to R.Z.H, and a Helen Lyng White postdoctoral fellowship to A.T. G.S. is a New York Stem Cell Foundation – Robertson Investigator.

Authors Contributions

L.L.O. conceptualized the study, supervised research, designed and guided experiments, interpreted data, helped assemble figures, and revised the manuscript. P-E.Y.N. helped design and performed experiments, data analysis, interpreted data, assembled figures, and wrote the manuscript. S.R.M. performed mouse surgery required for retrograde tracing, helped guide experiments, and contributed to the Piezo2 analysis. A.T. helped inject mice for retrograde tracing experiment. A.T. and M.G. dissected, imaged and analyzed DRGs data. G.S. interpreted retrograde tracing data and supervised A.T. and M.G. research. R.Z.H. performed NFH, NPY/TH, and CGRP/TH immunostainings, interpreted the results, and assembled the associated figures. S.S. immunostained and quantified the CGRP/TH innervation of glomeruli. R.Z.H. supervised S.S. All authors contributed to the manuscript text relevant to their contributions.

References

Banek, C. T., Knuepfer, M. M., Foss, J. D., Fiege, J. K., Asirvatham-Jeyaraj, N., Van Helden, D., Shimizu, Y., & Osborn, J. W. (2016). Resting Afferent Renal Nerve Discharge and Renal Inflammation. *Hypertension*, *68*(6), 1415-1423. https://doi.org/10.1161/hypertensionaha.116.07850

Barajas, L., Liu, L., & Powers, K. (1992). Anatomy of the renal innervation: intrarenal aspects and ganglia of origin. *Can J Physiol Pharmacol*, *70*(5), 735-749. https://doi.org/10.1139/y92-098

Barajas, L., Powers, K., & Wang, P. (1984). Innervation of the renal cortical tubules: a quantitative study. *Am J Physiol*, *247*(1 Pt 2), F50-60. https://doi.org/10.1152/ajprenal.1984.247.1.F50

Bell, C., & McLachlan, E. M. (1982). Dopaminergic neurons in sympathetic ganglia of the dog. *Proceedings of the Royal Society of London. Series B. Biological Sciences*, *215*(1199), 175-190. https://doi.org/10.1098/rspb.1982.0036

Bhatt, D. L., Vaduganathan, M., Kandzari, D. E., Leon, M. B., Rocha-Singh, K., Townsend, R. R., Katzen, B. T., Oparil, S., Brar, S., DeBruin, V., Fahy, M., Bakris, G. L., & Investigators, S. H.-S. C. (2022). Long-term outcomes after catheter-based renal artery denervation for resistant hypertension: final follow-up of the randomised SYMPLICITY HTN-3 Trial. *Lancet*, *400*(10361), 1405-1416. https://doi.org/10.1016/S0140-6736(22)01787-1

Bozic, M., de Rooij, J., Parisi, E., Ortega, M. R., Fernandez, E., & Valdivielso, J. M. (2011). Glutamatergic signaling maintains the epithelial phenotype of proximal tubular cells. *J Am Soc Nephrol*, *22*(6), 1099-1111. https://doi.org/10.1681/ASN.2010070701

Brading, A. (1999). *The autonomic nervous system and its effectors*. Blackwell Science.

Booth LC, May CN, Yao ST. The role of the renal afferent and efferent nerve fibers in heart failure. Front Physiol. 2015 Oct 1;6:270. doi: 10.3389/fphys.2015.00270.

Chan, K.Y., Jang, M.J., Yoo, B.B., Greenbaum, A., Ravi, N., Wu, W.L., Sánchez-Guardado, L., Lois, C., Mazmanian, S.K., Deverman, B.E., & Gradinaru, V. (2017). Engineered AAVs for efficient noninvasive gene delivery to the central and peripheral nervous systems. *Nat Neurosci*. 20(8):1172-1179. https://doi.org/10.1038/nn.4593

Cheng, X., Zhang, Y., Chen, R., Qian, S., Lv, H., Liu, X., & Zeng, S. (2022). Anatomical Evidence for Parasympathetic Innervation of the Renal Vasculature and Pelvis. *J Am Soc Nephrol*, *33*(12), 2194-2210. https://doi.org/10.1681/ASN.2021111518

Chin, L. S., et al. (1995). "Impairment of axonal development and of synaptogenesis in hippocampal neurons of synapsin I-deficient mice." Proc Natl Acad Sci U S A 92(20): 9230-9234.

Christianson, J. A., Liang, R., Ustinova, E. E., Davis, B. M., Fraser, M. O., & Pezzone, M. A. (2007). Convergence of bladder and colon sensory innervation occurs at the primary afferent level. *Pain*, *128*(3), 235-243. https://doi.org/10.1016/j.pain.2006.09.023

Combes, A. N., Phipson, B., Lawlor, K. T., Dorison, A., Patrick, R., Zappia, L., Harvey, R. P., Oshlack, A., & Little, M. H. (2019). Single cell analysis of the developing mouse kidney provides deeper insight into marker gene expression and ligand-receptor crosstalk. *Development*, *146*(12), dev178673. https://doi.org/10.1242/dev.178673

Coste, B., et al. (2010). "Piezo1 and Piezo2 are essential components of distinct mechanically activated cation channels." Science 330(6000): 55-60.

880 Daniel, E., Azizoglu, D. B., Ryan, A. R., Walji, T. A., Chaney, C. P., Sutton, G. I., Carroll, T. J.,
881 Marciano, D. K., & Cleaver, O. (2018). Spatiotemporal heterogeneity and patterning of
882 developing renal blood vessels. *Angiogenesis*, *21*(3), 617-634.
883 https://doi.org/10.1007/s10456-018-9612-y
884 Denton, K. M., Luff, S. E., Shweta, A., & Anderson, W. P. (2004). DIFFERENTIAL NEURAL CONTROL
885 OF GLOMERULAR ULTRAFILTRATION. *Clinical and Experimental Pharmacology and*
886 *Physiology*, *31*(5-6), 380-386. https://doi.org/10.1111/j.1440-1681.2004.04002.x
887 Dibona, G. F. (2000). Nervous Kidney. *Hypertension*, *36*(6), 1083-1088.
888 https://doi.org/10.1161/01.hyp.36.6.1083
889 DiBona, G. F., & Kopp, U. C. (1997). Neural control of renal function. *Physiol Rev*, *77*(1), 75-197.
890 https://doi.org/10.1152/physrev.1997.77.1.75
891 DiBona, G. F. (2004). "The sympathetic nervous system and hypertension: recent developments."
892 Hypertension 43(2): 147-150.
893 Donovan, M. K., Wyss, J. M., & Winternitz, S. R. (1983). Localization of renal sensory neurons
894 using the fluorescent dye technique. *Brain Res*, *259*(1), 119-122.
895 https://doi.org/10.1016/0006-8993(83)91072-7
896 Ernsberger, U., Deller, T., & Rohrer, H. (2020). The diversity of neuronal phenotypes in rodent
897 and human autonomic ganglia. *Cell Tissue Res*, *382*(2), 201-231.
898 https://doi.org/10.1007/s00441-020-03279-6
899 Esler, M. D., Krum, H., Schlaich, M., Schmieder, R. E., Bohm, M., Sobotka, P. A., & Symplicity, H.
900 T. N. I. (2012). Renal sympathetic denervation for treatment of drug-resistant
901 hypertension: one-year results from the Symplicity HTN-2 randomized, controlled trial.
902 *Circulation*, *126*(25), 2976-2982. https://doi.org/10.1161/CIRCULATIONAHA.112.130880
903 Ferguson, M., Ryan, G. B., & Bell, C. (1986). Localization of sympathetic and sensory neurons
904 innervating the rat kidney. *Journal of the Autonomic Nervous System*, *16*(4), 279-288.
905 https://doi.org/10.1016/0165-1838(86)90034-2
906 Ferguson, M., Ryan, G. B., & Bell, C. (1988). The innervation of the renal cortex in the dog. *Cell*
907 *and Tissue Research*, *253*(3). https://doi.org/10.1007/bf00219744
908 Fujisawa, Y., Nagai, Y., Lei, B., Nakano, D., Fukui, T., Hitomi, H., Mori, H., Masaki, T., & Nishiyama,
909 A. (2011). Roles of central renin-angiotensin system and afferent renal nerve in the
910 control of systemic hemodynamics in rats. *Hypertension Research*, *34*(11), 1228-1232.
911 https://doi.org/10.1038/hr.2011.115
912 Ginty, N. O. G. a. D. D. (2004). Heterogeneous Requirement of NGF for Sympathetic Target
913 Innervation In Vivo. *Journal of Neuroscience*, *24*(3), 743-751.
914 https://doi.org/10.1523/jneurosci.4523-03.2004
915 Glebova, N. O., & Ginty, D. D. (2005). GROWTH AND SURVIVAL SIGNALS CONTROLLING
916 SYMPATHETIC NERVOUS SYSTEM DEVELOPMENT. *Annual Review of Neuroscience*, *28*(1),
917 191-222. https://doi.org/10.1146/annurev.neuro.28.061604.135659
918 Golden, J. P., Hoshi, M., Nassar, M. A., Enomoto, H., Wood, J. N., Milbrandt, J., Gereau, R. W. t.,
919 Johnson, E. M., Jr., & Jain, S. (2010). RET signaling is required for survival and normal
920 function of nonpeptidergic nociceptors. *J Neurosci*, *30*(11), 3983-3994.
921 https://doi.org/10.1523/JNEUROSCI.5930-09.2010
922 Gu, Z., et al. (2016). "Complex heatmaps reveal patterns and correlations in multidimensional
923 genomic data." Bioinformatics 32(18): 2847-2849.

924 Hill, R.Z., Shirvan, S., Burquez, S., Dubin, A.E., Servin-Vences, M.R., Miner, J.H., & Patapoutian, A.
925 (2023). Renal mechanotransduction is an essential regulator of renin. *bioRxiv,*
926 2023.11.04.565646; doi: https://doi.org/10.1101/2023.11.04.565646.
927 Howard, M. J. (2005). Mechanisms and perspectives on differentiation of autonomic neurons.
928 *Dev Biol*, *277*(2), 271-286. https://doi.org/10.1016/j.ydbio.2004.09.034
929 Honeycutt, S. E., N'Guetta, P.Y., Hardesty, D.M., Xiong, Y., Cooper, S.L., Stevenson, M.J., &
930 O'Brien, L.L. (2023). Netrin-1 directs vascular patterning and maturity in the developing
931 kidney. *Development*. doi: 10.1242/dev.201886. PMID: 37818607
932 Kopp, U. C. (2015). Role of renal sensory nerves in physiological and pathophysiological
933 conditions. *Am J Physiol Regul Integr Comp Physiol*, *308*(2), R79-95.
934 https://doi.org/10.1152/ajpregu.00351.2014
935 Krum, H., Schlaich, M., & Sobotka, P. (2013). Renal Sympathetic Nerve Ablation for Treatment-
936 Resistant Hypertension. *British Journal of Clinical Pharmacology*, n/a-n/a.
937 https://doi.org/10.1111/bcp.12171
938 Krum, H., Schlaich, M. P., Sobotka, P. A., Bohm, M., Mahfoud, F., Rocha-Singh, K., Katholi, R., &
939 Esler, M. D. (2014). Percutaneous renal denervation in patients with treatment-resistant
940 hypertension: final 3-year report of the Symplicity HTN-1 study. *Lancet*, *383*(9917), 622-
941 629. https://doi.org/10.1016/S0140-6736(13)62192-3
942 Kuo, D. C., de Groat, W. C., & Nadelhaft, I. (1982). Origin of sympathetic efferent axons in the
943 renal nerves of the cat. *Neurosci Lett*, *29*(3), 213-218. https://doi.org/10.1016/0304-
944 3940(82)90319-6
945 Knuepfer M, Schramm LP. The conduction velocities and spinal projections of single renal afferent
946 fibers in the rat. Brain Res 435: pp. 167–73, 1987. 10.1016/0006-8993(87)91598-8.
947 Lee, S., Yang, G., Xiang, W., & Bushman, W. (2016). Retrograde double-labeling demonstrates
948 convergent afferent innervation of the prostate and bladder. *Prostate*, *76*(8), 767-775.
949 https://doi.org/10.1002/pros.23170
950 Lam, R. M., et al. (2023). "PIEZO2 and perineal mechanosensation are essential for sexual
951 function." Science 381(6660): 906-910.
952 Luo, P. M., et al. (2023). "Stromal netrin-1 coordinates renal arteriogenesis and mural cell
953 differentiation." Development.
954 Malpas, S. C. (2010). Sympathetic nervous system overactivity and its role in the development of
955 cardiovascular disease. *Physiol Rev*, *90*(2), 513-557.
956 https://doi.org/10.1152/physrev.00007.2009
957 May, C. N., Frithiof, R., Hood, S. G., McAllen, R. M., McKinley, M. J., & Ramchandra, R. (2010).
958 Specific control of sympathetic nerve activity to the mammalian heart and kidney.
959 *Experimental Physiology*, *95*(1), 34-40. https://doi.org/10.1113/expphysiol.2008.046342
960 McMahon, A. P. (2016). Development of the Mammalian Kidney. In (pp. 31-64). Elsevier.
961 https://doi.org/10.1016/bs.ctdb.2015.10.010
962 Meerschaert, K. A., Adelman, P. C., Friedman, R. L., Albers, K. M., Koerber, H. R., & Davis, B. M.
963 (2020). Unique Molecular Characteristics of Visceral Afferents Arising from Different
964 Levels of the Neuraxis: Location of Afferent Somata Predicts Function and Stimulus
965 Detection Modalities. *J Neurosci*, *40*(38), 7216-7228.
966 https://doi.org/10.1523/JNEUROSCI.1426-20.2020

967 Mitchell, G. A. (1950). The nerve supply of the kidneys. *Acta Anat (Basel)*, *10*(1-2), 1-37.
968 https://doi.org/10.1159/000140455
969 Marshall, K. L., et al. (2020). "PIEZO2 in sensory neurons and urothelial cells coordinates
970 urination." Nature 588(7837): 290-295.
971 Mochida, Y., et al. (2022). "Piezo2 expression and its alteration by mechanical forces in mouse
972 mesangial cells and renin-producing cells." Sci Rep 12(1): 4197.
973 Osborn, J. W., & Foss, J. D. (2017). Renal Nerves and Long-Term Control of Arterial Pressure.
974 *Compr Physiol*, *7*(2), 263-320. https://doi.org/10.1002/cphy.c150047
975 Osborn, J. W., Tyshynsky, R., & Vulchanova, L. (2021). Function of Renal Nerves in Kidney
976 Physiology and Pathophysiology. *Annu Rev Physiol*, *83*, 429-450.
977 https://doi.org/10.1146/annurev-physiol-031620-091656
978 Ong, J., et al. (2019). "Renal sensory nerves increase sympathetic nerve activity and blood
979 pressure in 2-kidney 1-clip hypertensive mice." J Neurophysiol 122(1): 358-367.
980 Renier, N., Wu, Z., David, Yang, J., Ariel, P., & Tessier-Lavigne, M. (2014). iDISCO: A Simple, Rapid
981 Method to Immunolabel Large Tissue Samples for Volume Imaging. *Cell*, *159*(4), 896-910.
982 https://doi.org/10.1016/j.cell.2014.10.010
983 Sata, Y., Head, G. A., Denton, K., May, C. N., & Schlaich, M. P. (2018). Role of the Sympathetic
984 Nervous System and Its Modulation in Renal Hypertension. *Front Med (Lausanne)*, *5*, 82.
985 https://doi.org/10.3389/fmed.2018.00082
986 Schlaich, M. P., Sobotka, P. A., Krum, H., Lambert, E., & Esler, M. D. (2009). Renal Sympathetic-
987 Nerve Ablation for Uncontrolled Hypertension. *New England Journal of Medicine*, *361*(9),
988 932-934. https://doi.org/10.1056/nejmc0904179
989 Simon OR, Schramm LP (1983) Spinal Superfusion of Dopamine Excites Renal Sympathetic Nerve
990 Activity. Neuropharmacology 22:287–293.
991 Smith-Anttila, C. J. A., Morrison, V., & Keast, J. R. (2021). Spatiotemporal mapping of sensory and
992 motor innervation of the embryonic and postnatal mouse urinary bladder. *Dev Biol*, *476*,
993 18-32. https://doi.org/10.1016/j.ydbio.2021.03.008
994 Smyth, I. M. (2021). Monkeying about with Nephron Formation. *J Am Soc Nephrol*, *32*(5), 1011-
995 1013. https://doi.org/10.1681/ASN.2021030320
996 Symplicity, H. T. N. I., Esler, M. D., Krum, H., Sobotka, P. A., Schlaich, M. P., Schmieder, R. E., &
997 Bohm, M. (2010). Renal sympathetic denervation in patients with treatment-resistant
998 hypertension (The Symplicity HTN-2 Trial): a randomised controlled trial. *Lancet*,
999 *376*(9756), 1903-1909. https://doi.org/10.1016/S0140-6736(10)62039-9
1000 Stella A, Zanchetti A (1991) Functional Role of Renal Afferents. 71:659–682.
1001 Stocker, S. D. and J. B. Sullivan (2023). "Deletion of the Transient Receptor Potential Vanilloid 1
1002 Channel Attenuates Sympathoexcitation and Hypertension and Improves Glomerular
1003 Filtration Rate in 2-Kidney-1-Clip Rats." Hypertension 80(8): 1671-1682.
1004 Tarnick, J., et al. (2023). "Innervation of the developing kidney in vivo and in vitro." Biol Open
1005 12(8).
1006 Townsend, R. R., Mahfoud, F., Kandzari, D. E., Kario, K., Pocock, S., Weber, M. A., Ewen, S.,
1007 Tsioufis, K., Tousoulis, D., Sharp, A. S. P., Watkinson, A. F., Schmieder, R. E., Schmid, A.,
1008 Choi, J. W., East, C., Walton, A., Hopper, I., Cohen, D. L., Wilensky, R., . . . investigators*,
1009 S. H.-O. M. t. (2017). Catheter-based renal denervation in patients with uncontrolled
1010 hypertension in the absence of antihypertensive medications (SPYRAL HTN-OFF MED): a

1011 randomised, sham-controlled, proof-of-concept trial. *Lancet*, *390*(10108), 2160-2170.
1012 https://doi.org/10.1016/S0140-6736(17)32281-X
1013 Tyshynsky, R., et al. (2023). "Periglomerular afferent innervation of the mouse renal cortex."
1014 Front Neurosci 17: 974197.
1015 Torres, H., et al. (2021). "Sympathetic innervation of the mouse kidney and liver arising from
1016 prevertebral ganglia." Am J Physiol Regul Integr Comp Physiol 321(3): R328-R337.
1017 Tiniakos, D., et al. (2004). "Ontogeny of intrinsic innervation in the human kidney." Anat Embryol
1018 (Berl) 209(1): 41-47.
1019 Veelken, R., Vogel, E.-M., Hilgers, K., Amann, K., Hartner, A., Sass, G., Neuhuber, W., & Tiegs, G.
1020 (2008). Autonomic Renal Denervation Ameliorates Experimental Glomerulonephritis.
1021 *Journal of the American Society of Nephrology*, *19*(7), 1371-1378.
1022 https://doi.org/10.1681/asn.2007050552
1023 Wickham, H. (2009) Ggplot2: Elegant Graphics for Data Analysis. 2nd Edition, Springer, New York.
1024 https://doi.org/10.1007/978-0-387-98141-3
1025 Weiss, M. L. and S. I. Chowdhury (1998). "The renal afferent pathways in the rat: a pseudorabies
1026 virus study." Brain Res 812(1-2): 227-241.
1027 Xiao, L., Kirabo, A., Wu, J., Saleh, M. A., Zhu, L., Wang, F., Takahashi, T., Loperena, R., Foss, J. D.,
1028 Mernaugh, R. L., Chen, W., Roberts, J., Osborn, J. W., Itani, H. A., & Harrison, D. G. (2015).
1029 Renal Denervation Prevents Immune Cell Activation and Renal Inflammation in
1030 Angiotensin II–Induced Hypertension. *Circulation Research*, *117*(6), 547-557.
1031 https://doi.org/10.1161/circresaha.115.306010
1032 Zheng, M., Chen, R., Chen, H., Zhang, Y., Chen, J., Lin, P., Lan, Q., Yuan, Q., Lai, Y., Jiang, X., Pan,
1033 X., & Liu, N. (2018). Netrin-1 Promotes Synaptic Formation and Axonal Regeneration via
1034 JNK1/c-Jun Pathway after the Middle Cerebral Artery Occlusion. *Front Cell Neurosci*, *12*,
1035 13. https://doi.org/10.3389/fncel.2018.00013
1036
1037
1038
1039
1040
1041
1042
1043
1044
1045
1046
1047
1048

1049 **Figure 1. Kidney innervation commences at E13.5 as axons follow the**
1050 **differentiating arteries and continue to branch throughout development. (A)** Pan-
1051 neuronal labeling (TUBB3, green) of an E12.5 urogenital system (UGS) shows that renal
1052 nerves are absent in the kidney at E12.5 as shown by immunostaining of the branching
1053 ureteric bud (cytokeratin, yellow). Ganglion and some postganglionic nerve fibers track
1054 along the descending aorta shown by smooth muscle actin (SMA, magenta). **(B)** Pan-
1055 neuronal labeling (TUBB3, green) of an E13.5 UGS shows that axons begin to innervate
1056 the kidney following the SMA+ vascular mural cells (magenta) of the developing arteries
1057 (white arrowhead, zoomed image). CD31 (yellow) highlights the extensive endothelial
1058 network that has formed but is yet to be coated with mural cells. **(C)** Axonal projections
1059 (TUBB3, green) continue to grow and branch following the developing arterial tree (SMA,
1060 magenta) at E16.5. Cytokeratin (yellow) marks the collecting duct system. Multiple axon
1061 bundles can be observed on an artery (white arrowhead, zoomed image). **(D)** By E18.5,
1062 axons (TUBB3, green) have undergone extensive growth with the arterial tree (SMA,
1063 magenta) and additional interstitial branching as the nerves navigate towards and around
1064 kidney structures such as glomeruli (NPHS2, yellow; white arrowhead, zoomed image) A
1065 minimum of n=3 kidneys were analyzed for each stage.
1066
1067 **Figure 2: Nociceptive sensory afferent nerves innervate the developing kidney. (A)**
1068 Wholemount immunostain of an E16.5 *Trpv1*$^{Cre/+}$;*R26*$^{tdTomato/+}$ kidney showing tdTomato+
1069 (magenta) axons colocalizing with the pan-neuronal marker TUBB3 (green). A magnified
1070 inset from the merged shows tdTomato^{+} axons overlapping with TUBB3. **(B)**
1071 *Trpv1*$^{Cre/+}$;*R26*$^{tdTomato/+}$ P1 kidney section showing native tdTomato signal (magenta) with
1072 immunostained proximal tubules (LRP2, green) and epithelium (ECAD, yellow).
1073 TdTomato+ axons navigate around and closely associate with these structures (white
1074 arrowheads). **(C)** *Trpv1*$^{Cre/+}$;*R26*$^{tdTomato/+}$ P1 kidney section showing native tdTomato
1075 signal (magenta) with immunostained podocytes (to mark glomeruli, NPHS2, green) and
1076 endothelium (CD31, yellow). TdTomato+ axons extend along the vasculature and
1077 associate with glomeruli (white arrowhead). A minimum of n=3 kidneys were analyzed for
1078 each stage.
1079

1080 **Figure 3: Peptidergic and mechanosensory afferent nerves are present in the**
1081 **developing kidney. (A)** E15.5 kidney section immunostained for the neuropeptide
1082 CGRP^{+} (magenta) and pan-neuronal marker TUBB3 (green). CGRP^{+} nerves mainly
1083 associate with the kidney vasculature (CD31, yellow; white arrowhead) at this stage. **(B)**
1084 Sections of *Pod-Cre$^{tg/+}$;R26$^{tdTomato/tdTomato}$* P0 kidneys immunostained for CGRP^{+}
1085 (magenta). CGRP+ axons are found near (white arrowhead) glomeruli (tdTomato, green)
1086 and close to proximal tubules (LRP2, yellow). **(C)** Adult kidney section immunostained for
1087 CGRP (magenta) and colocalized with TUBB3 (green) shows CGRP^{+} axons closely
1088 associating with the vasculature (CD31, yellow) and in close proximity to glomeruli (white
1089 arrowhead). **(D)** E18.5 kidney section immunostained for substance P (SubP, magenta)
1090 shows overlap with TUBB3 (green). SubP^{+} nerves were found associated with the
1091 vasculature (CD31, yellow, white arrowhead). **(E)** Adult kidney section immunostained for
1092 SubP^{+} (magenta) and TUBB3 (green) shows SubP+ nerves along the vasculature (CD31,
1093 yellow) and in close proximity to glomeruli (white arrowhead). **(F)** E15.5 kidney section
1094 immunostained for PIEZO2 (magenta) and TUBB3 (green) show PIEZO2+ nerves
1095 associating with the vasculature (CD31, yellow; white arrowhead). **(G)** Sections of *Pod-*
1096 *Cre$^{tg/+}$;R26$^{tdTomato/tdTomato}$* P0 kidneys immunostained for PIEZO2 (magenta) show
1097 PIEZO2+ nerves closely associating (white arrowheads) with glomeruli (tdTomato, green)
1098 and proximal tubules (LRP2, yellow). A minimum of n=3 kidneys were analyzed for each
1099 stage.
1100
1101 **Figure 4: CTB retrograde tracing shows axon trajectories and labeling of thoracic,**
1102 **lumbar, and sacral DRGs. (A)** Schematic of retrograde tracing injection and timeline.
1103 CTB-555 was injected into the right kidney of adult mice. Three days following the
1104 injection both kidneys were dissected as well as the ipsilateral DRGs (injected side) and
1105 contralateral DRGs (non-injected side). **(B)** Sensory innervation primarily traces in the
1106 ipsilateral DRGs to the lower thoracic region (T10-T13), lumbar region (L1-L6), and sacral
1107 region (S1-S2). Tracing to the contralateral DRGs was observed in the upper lumbar
1108 region of L1 and L2. n=4 males and n=4 females, Scale bar =50μm. **(C)** Ipsilateral and
1109 contralateral kidney sections of CTB-injected kidneys. Immunostaining of the ipsilateral
1110 kidney section showed CTB^{+} staining (magenta) colocalizing with TUBB3 (green) near

1111 glomeruli (CD31, yellow, arrowhead) and vasculature (CD31, yellow). CTB^{+} staining
1112 (magenta, arrowhead) colocalized with TUBB3 (green) near vasculature (CD31, yellow)
1113 in the contralateral (non-injected) kidney. **(D)** Schematic representation of the spinal level
1114 and DRG origin of kidney sensory afferent innervation.
1115
1116 **Figure 5: Noradrenergic sympathetic nerves innervate the developing kidney. (A)**
1117 E14.5 wholemount immunostained kidney labeled with tyrosine hydroxylase (TH,
1118 magenta) shows that the first innervating axons (TUBB3, green) are TH+. Cytokeratin
1119 (yellow) marks the developing collecting duct system. **(B)** P0 wholemount immunostained
1120 kidney labeled with TH (magenta) shows that the TH+ nerves have branched extensively
1121 alongside the arterial tree (SMA, green). LRP2 marks the proximal tubules (yellow) and
1122 the magnified inset shows TH^{+} nerves (magenta) navigating around and in close proximity
1123 to proximal tubules (white arrowheads). **(C)** E15.5 kidney section immunostained for TH
1124 (magenta) and TUBB3 (green) shows TH+ axons around the vasculature (CD31, yellow;
1125 white arrowhead). **(D)** Sections of *Pod-Cre*$^{tg/+}$*;R26*$^{tdTomato/tdTomato}$ P0 kidneys
1126 immunostained for TH (magenta) show TH^{+} axons near glomeruli (tdTomato, green; white
1127 arrowhead) and proximal tubules (LRP2, yellow)**.** A minimum of n=3 kidneys were
1128 analyzed for each stage. **(E)** Image of the adult kidney cortex immunostained for the
1129 neuropeptide NPY (magenta), TH (green), and the nuclear counterstain DAPI (blue).
1130 Glomeruli are encircled in white dotted lines. No TH^{+}/NPY^{-} fibers were observed. Image
1131 is representative of n=2 male mice.
1132
1133 **Figure 6: Nerves form putative neuroeffector-junctions with kidney targets during**
1134 **development. (A)** Immunostaining of E14.5 kidney sections for synapsin I (SYN1,
1135 magenta) shows overlap with TUBB3 (green) and association of axons with the main
1136 artery (CD31, yellow; white arrowhead). **(B)** E15.5 kidney sections immunostained for
1137 SYN1 (magenta) and TUBB3 (green) similarly show SYN1^{+} nerves positive around the
1138 vasculature (CD31, yellow). **(C)** Sections of *Pod-Cre*$^{tg/+}$*;R26*$^{tdTomato/tdTomato}$ P0 kidneys
1139 immunostained for SYN1 (magenta) show SYN1+ axons (TUBB3, green) near glomeruli
1140 (tdTomato, green; white arrowheads, top panel) and proximal tubules (LRP2, yellow;
1141 White arrowhead, bottom panel). **(D)** Sections of *Pod-Cre*$^{tg/+}$*;R26*$^{tdTomato/tdTomato}$ adult

1142 kidneys immunostained for SYN1 (magenta) show SYN1+ axons (TUBB3, green) along
1143 the arterioles near glomeruli (tdTomato, green; white arrowhead). A minimum of n=3
1144 kidneys were analyzed for each stage.
1145
1146 **Figure 7: Sympathetic and sensory nerves show similar structural associations in**
1147 **the adult human kidney. (A)** Adult human kidney sections immunostained for TH^+
1148 sympathetic nerves (green) can be observed associating with glomeruli shown by
1149 Podocalyxin (magenta; top panel, white arrowhead) and in close proximity to epithelial
1150 structures (ECAD, yellow; bottom panel, white arrowhead). **(B)** Adult human kidney
1151 sections immunostained for PIEZO2 (magenta) show $PIEZO2^+$ overlapping with TUBB3
1152 (green) associating with glomeruli (Podocalyxin, yellow; white arrowhead, top panel) and
1153 the vasculature (Podocalyxin, yellow; white arrowhead, middle panel). PIEZO2+ sensory
1154 nerves were also observed near epithelial structures (LRP, green; ECAD, yellow; white
1155 arrowhead, bottom panel). **(C)** Adult human kidney sections immunostained for SYN1
1156 (green) show SYN1+ axons near glomeruli (Podocalyxin, magenta; white arrowhead, top
1157 panel) and epithelial structures (ECAD, yellow; white arrowhead, bottom panel).
1158
1159 **Figure S1: Innervation of the embryonic and postnatal kidney. (A)** Wholemount
1160 immunostain of an E14.5 kidney for TUBB3 (green), SMA (red), and CD31 (grey). Axons
1161 track closely with the developing arteries despite the presence of an extensive CD31+
1162 endothelial network. (**B)** Wholemount immunostain of a P0 kidney for TUBB3 (green),
1163 NPHS2 (podocytes, magenta), and LRP2 (proximal tubules, yellow). The neuronal
1164 network continues to expand and navigate towards and around kidney structures. **(C)**
1165 Wholemount immunostain of a P0 kidney for TUBB3 (green), SMA (red), and NPHS2
1166 (podocytes, grey). The neuronal network has continued to grow as the vasculature
1167 expands and the last wave of nephrons differentiate.
1168
1169 **Figure S2: Axons associate with kidney structures during embryonic development**.
1170 (**A)** Image of an E18.5 kidney section immunostained for vasculature (SMA, magenta)
1171 and nerves (TUBB3, green). Axons are tightly associated with the SMA+ vasculature. **(B)**
1172 Image of an E18.5 kidney section immunostained for nerves (TUBB3, green) and

1173 glomeruli (NPHS2, magenta). Axons approach the glomeruli and associate with the
1174 Bowman's capsule as they navigate through the kidney. **(C)** Image of an E18.5 kidney
1175 section immunostained for nerves (TUBB3, green) and tubule epithelium (ECAD,
1176 magenta). Axons are observed closely associating with ECAD$^+$ tubules. A minimum of
1177 n=3 kidneys were analyzed for each stage.
1178
1179 **Figure S3: Kidney peptidergic sensory innervation is delayed. (A)** E14.5 kidney
1180 sections immunostained for CGRP (magenta) shows that axons at this stage (TUBB3,
1181 green) that primarily associate with the vasculature (CD31, yellow) are not yet CGRP+.
1182 **(B)** E14.5 kidney sections immunostained for substance P (SubP, magenta) shows that
1183 axons at this stage (TUBB3, green) that primarily associate with the vasculature (CD31,
1184 yellow) are not yet SubP+.
1185
1186 **Figure S4: Myelinated NFH+ fibers sparsely innervate the kidney cortex and pelvis.**
1187 Image of the adult kidney cortex (left panel) immunostained for the CGRP (magenta), the
1188 cytoskeletal protein Neurofilament heavy polypeptide (NFH, green), and the nuclear
1189 counterstain DAPI (blue). A glomerulus is encircled in a white dotted line and the arrow
1190 indicates a single NFH+ fiber that does not approach the glomerulus and which is
1191 negative for CGRP immunoreactivity. These cortical NFH+ fibers were rarely observed.
1192 Image is representative of n=2 male mice. Image of the adult renal pelvis (right panel)
1193 immunostained for the CGRP (magenta), NFH (green), and DAPI (blue). The border of
1194 the pelvic urothelium is outlined with a white dashed line. NFH+ fibers were observed
1195 within the urothelium and occasionally these appeared to overlap with CGRP+, however,
1196 the density of CGRP immunoreactivity in the pelvis made it challenging to distinguish
1197 individual fibers. The asterisk (*) denotes a portion of nerve trunk comprised of multiple
1198 fibers containing both CGRP and NFH immunoreactivity. Image is representative of n=2
1199 male mice.
1200
1201 **Figure S5: pAAV-Flex retrograde tracing of PIEZO2$^+$ sensory nerves show labeling**
1202 **of lower thoracic and upper lumbar DRGs. (A)** Schematic of retrograde tracing
1203 injections and timeline. pAAV-Flex-tdTomato was injected into the right kidney of

1204 *Piezo2*$^{GFPCre/+}$ mice. Three weeks following ipsilateral (injected side) and contralateral
1205 (non-injected side) DRGs were collected for analysis. **(B)** PIEZO2^{+} renal sensory
1206 innervation primarily traces in the ipsilateral DRG in the lower thoracic region (T10-T13)
1207 and the upper lumbar region (L1-L2). Scale = 50μm. **(C)** Schematic representation of the
1208 spinal level and DRG origin of kidney PIEZO2+ sensory afferent innervation.
1209
1210 **Figure S6: Analysis of sensory and sympathetic innervation of glomeruli and the**
1211 **renal pelvis. (A)** Image of the adult kidney cortex (left) and the renal pelvis (right)
1212 immunostained for CGRP (magenta), TH (green), and the nuclear counterstain DAPI
1213 (blue). A glomerulus is encircled in a white dotted line and the border of the pelvic
1214 urothelium is outlined with a white dashed line. There is both sensory and sympathetic
1215 innervation of the arterioles adjacent to the glomerulus (white arrow) and the renal pelvis.
1216 Sensory nerves in the renal pelvis project more superficially into the urothelium than the
1217 sympathetic fibers. **(B)** Quantification of sensory and sympathetic innervation of glomeruli
1218 from n=3 animals (2 male and one female) expressed as a percentage of the total
1219 glomeruli. Total number of glomeruli analyzed is indicated above each bar. Error bars
1220 represent mean +/- SEM.
1221
1222 **Figure S7: The cholinergic marker VAChT labels axons in the developing kidney.**
1223 **(A)** E14.5 kidney sections immunostained for VAChT (magenta), TUBB3 (green), and
1224 CD31 (endothelium) show that axons (white arrowhead) are not positive for VAChT at
1225 this stage. VAChT signal is primarily background, non-specific signal. **(B)** E15.5 kidney
1226 sections immunostained for VAChT (magenta), TUBB3 (green), and CD31 (endothelium)
1227 show that VAChT signal (white arrowhead) is similar to TUBB3 axonal signal (green). **(C)**
1228 Sections of *Pod-Cre*$^{tg/+}$*;R26*$^{tdTomato/tdTomato}$ P0 kidneys immunostained for VAChT
1229 (magenta) show VAChT+ axons near glomeruli (tdTomato, green; white arrowheads, top
1230 panel) and proximal tubules (LRP2, yellow; White arrowhead, bottom panel). **(D)** Adult
1231 kidney sections immunostained for VAChT (magenta), TUBB3 (green), and CD31
1232 (endothelium) show that VAChT signal overlaps with TUBB3 and closely associates with
1233 the vasculature.
1234

1235 **Figure S8: Differential enrichment of adrenergic, purinergic, and post-synaptic**
1236 **markers within the different cell clusters of the E18.5 kidney (A)** Heatmaps showing
1237 relative enrichment of adrenergic receptors in the different kidney cell types (clusters)
1238 from E18.5 whole kidney scRNA-seq data (Combes et al., 2019). **(B)** Heatmaps showing
1239 relative enrichment of purinergic receptors in the different kidney cell types (clusters) at
1240 E18.5. **(C)** Heatmaps showing relative enrichment of post-synaptic markers in the
1241 different kidney cell types (clusters) at E18.5. The scale indicates log fold change relative
1242 to the other cell clusters. NP=nephron progenitor, PTA = pretubular aggregate, DT = distal
1243 tubule, CD = collecting duct, LoH=Loop of Henle, CnS=connecting segment. LogFC = log
1244 fold change differential expression.
1245
1246 **Suppl. Table 1: Wholemount tissue processing steps for iDISCO^{+} and light-sheet**
1247 **microscopy**
1248 **Suppl. Table 2: Imaging parameters utilized in this study**
1249 **Suppl. Table 3: List of primary antibodies used in this study**
1250 **Movie S1: Movie associated with Fig. 1A**
1251 **Movie S2: Movie associated with Fig. 1B**
1252 **Movie S3: Movie associated with Fig. 1B**
1253 **Movie S4: Movie associated with Fig. 1C**
1254 **Movie S5: Movie associated with Fig. 1D**
1255 **Movie S6: Movie associated with Fig. 8A**
1256 **Movie S7: Movie associated with Fig. 8C**

Figure 1

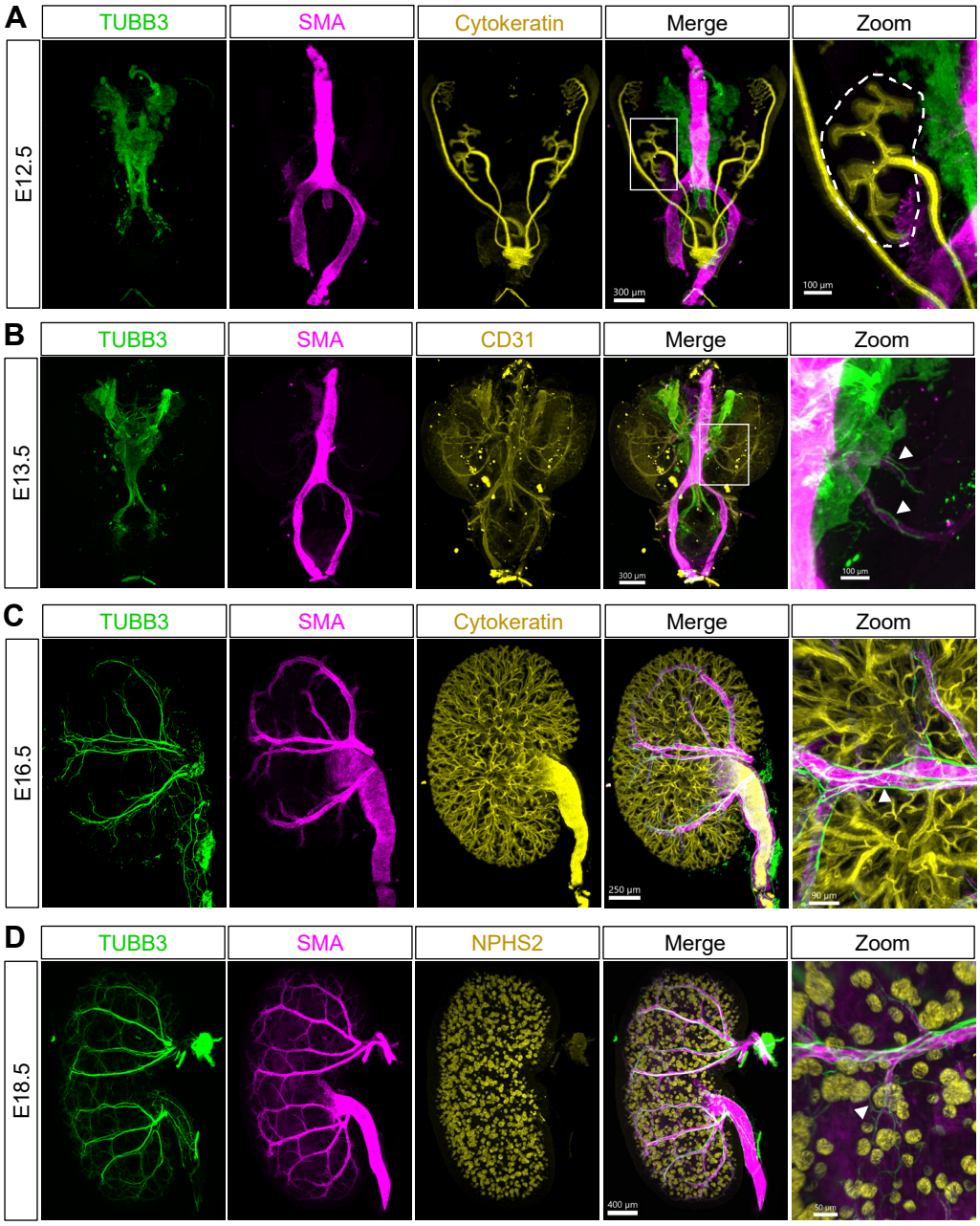
A
TUBB3
SMA
Cytokeratin
Merge
Zoom
E12.5
300 µm
100 µm
B
TUBB3
SMA
CD31
Merge
Zoom
E13.5
300 µm
100 µm
C
TUBB3
SMA
Cytokeratin
Merge
Zoom
E16.5
250 µm
90 µm
D
TUBB3
SMA
NPHS2
Merge
Zoom
E18.5
400 µm
50 µm

Figure 2

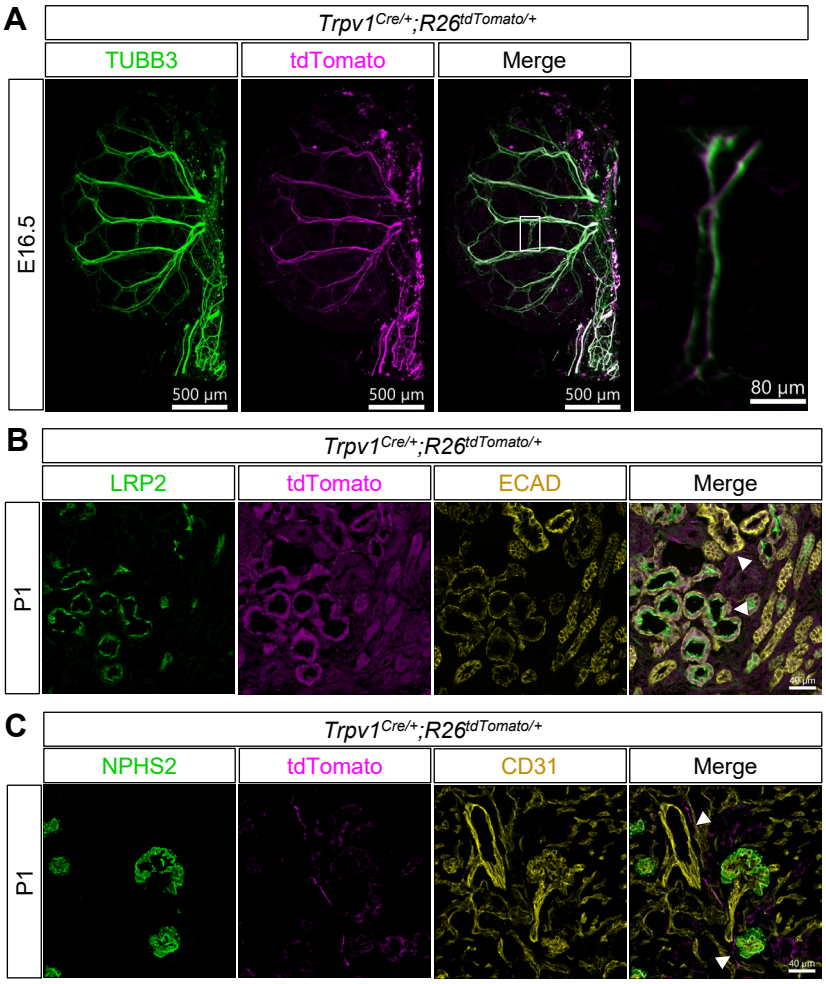
A
Trpv1Cre/+;R26tdTomato/+
TUBB3
tdTomato
Merge
E16.5
500 µm
500 µm
500 µm
80 µm
B
Trpv1Cre/+;R26tdTomato/+
LRP2
tdTomato
ECAD
Merge
P1
40 µm
C
Trpv1Cre/+;R26tdTomato/+
NPHS2
tdTomato
CD31
Merge
P1
40 µm

Figure 3

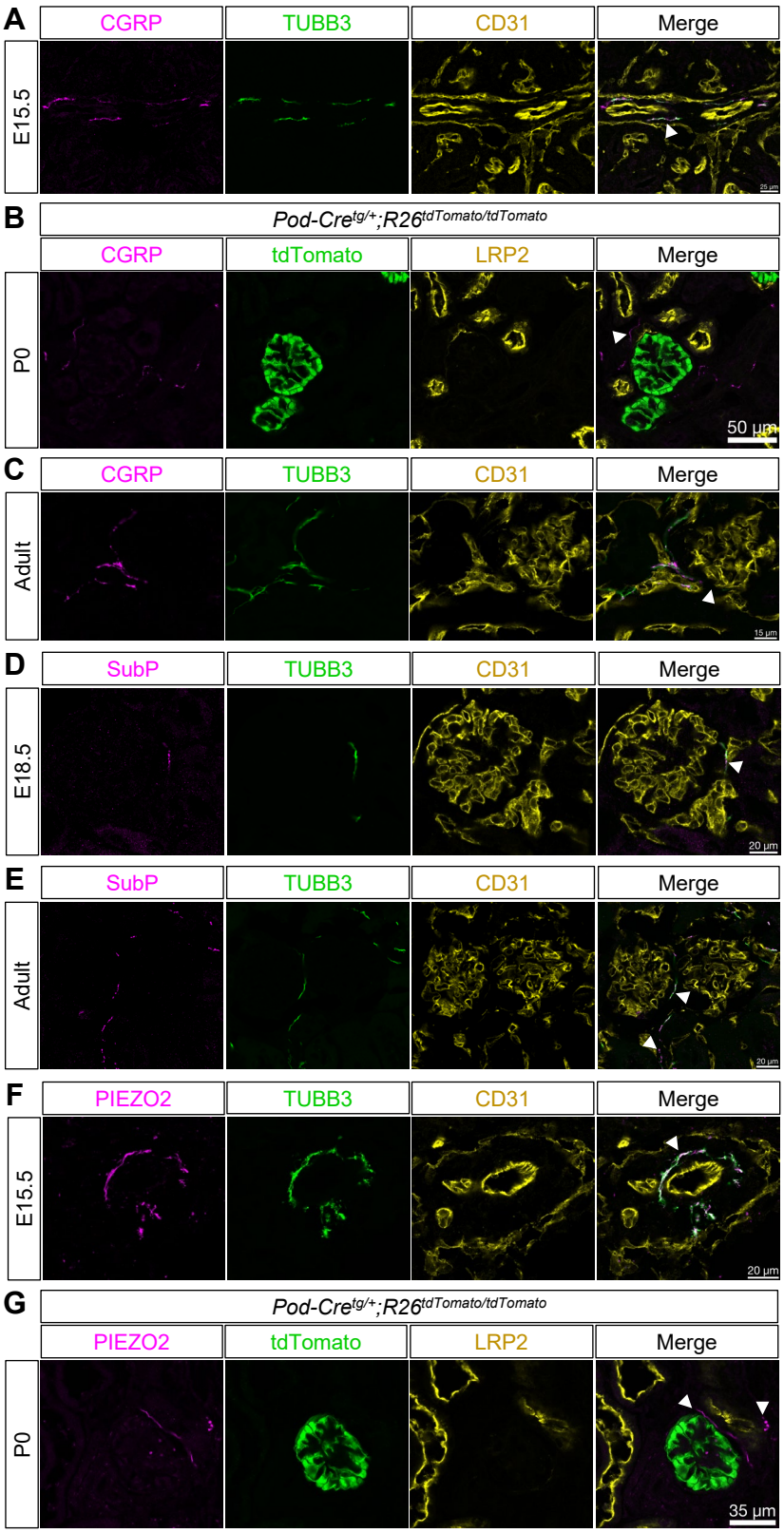
A
CGRP
TUBB3
CD31
Merge
E15.5
25 µm
B
Pod-Cretg/+;R26tdTomato/tdTomato
CGRP
tdTomato
LRP2
Merge
P0
50 µm
C
CGRP
TUBB3
CD31
Merge
Adult
15 µm
D
SubP
TUBB3
CD31
Merge
E18.5
20 µm
E
SubP
TUBB3
CD31
Merge
Adult
20 µm
F
PIEZO2
TUBB3
CD31
Merge
E15.5
20 µm
G
Pod-Cretg/+;R26tdTomato/tdTomato
PIEZO2
tdTomato
LRP2
Merge
P0
35 µm

Figure 4

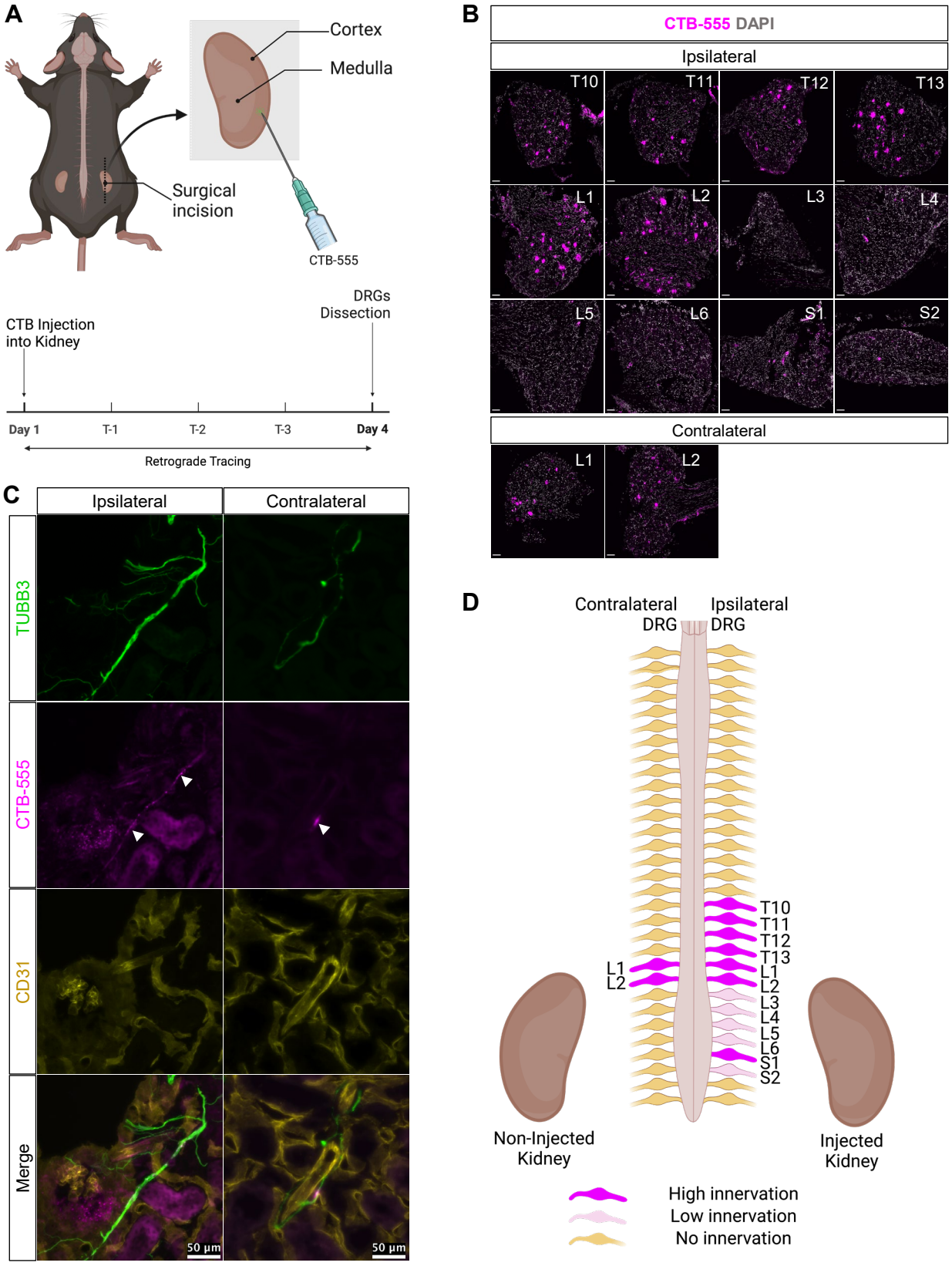
A
Cortex
Medulla
Surgical incision
CTB-555
DRGs Dissection
CTB Injection into Kidney
Day 1
T-1
T-2
T-3
Day 4
Retrograde Tracing
B
CTB-555 DAPI
Ipsilateral
T10
T11
T12
T13
L1
L2
L3
L4
L5
L6
S1
S2
Contralateral
L1
L2
C
Ipsilateral
Contralateral
TUBB3
CTB-555
CD31
Merge
50 µm
50 µm
D
Contralateral DRG
Ipsilateral DRG
T10
T11
T12
T13
L1
L2
L1
L2
L3
L4
L5
L6
S1
S2
Non-Injected Kidney
Injected Kidney
High innervation
Low innervation
No innervation

Figure 5

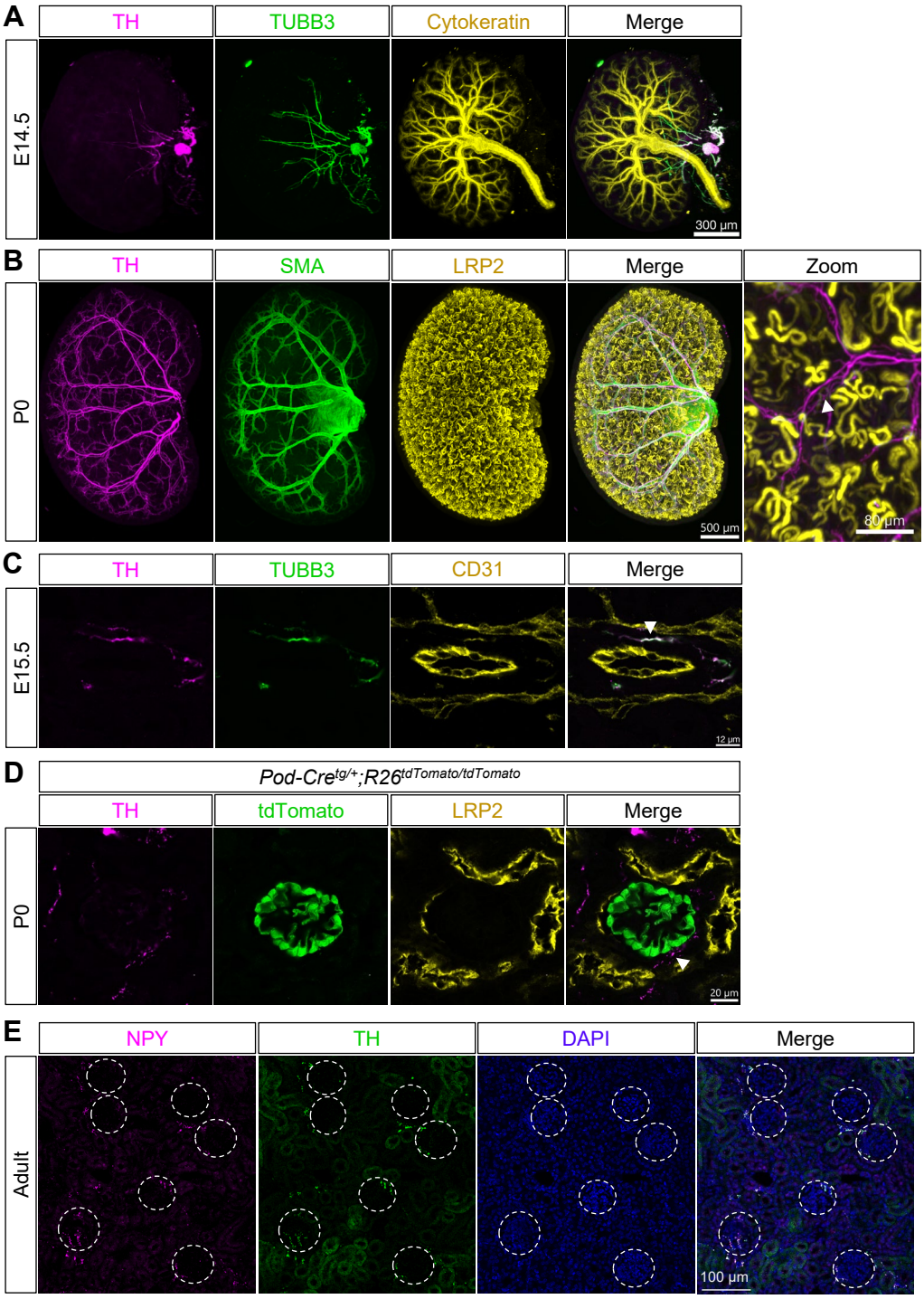
A
TH
TUBB3
Cytokeratin
Merge
E14.5
300 µm
B
TH
SMA
LRP2
Merge
Zoom
P0
500 µm
80 µm
C
TH
TUBB3
CD31
Merge
E15.5
12 µm
D
Pod-Cretg/+;R26tdTomato/tdTomato
TH
tdTomato
LRP2
Merge
P0
20 µm
E
NPY
TH
DAPI
Merge
Adult
100 µm

Figure 6

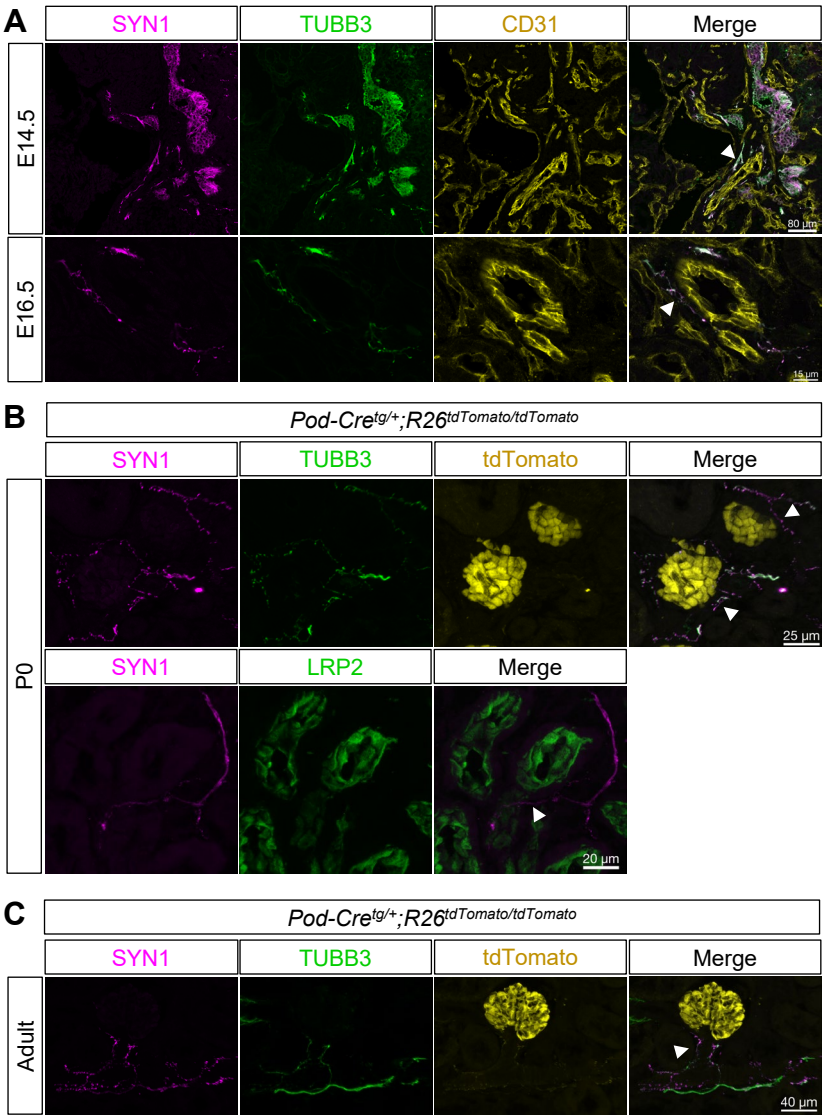
A
SYN1
TUBB3
CD31
Merge
E14.5
E16.5
80 µm
15 µm
B
Pod-Cretg/+;R26tdTomato/tdTomato
SYN1
TUBB3
tdTomato
Merge
P0
25 µm
SYN1
LRP2
Merge
20 µm
C
Pod-Cretg/+;R26tdTomato/tdTomato
SYN1
TUBB3
tdTomato
Merge
Adult
40 µm

Figure 7

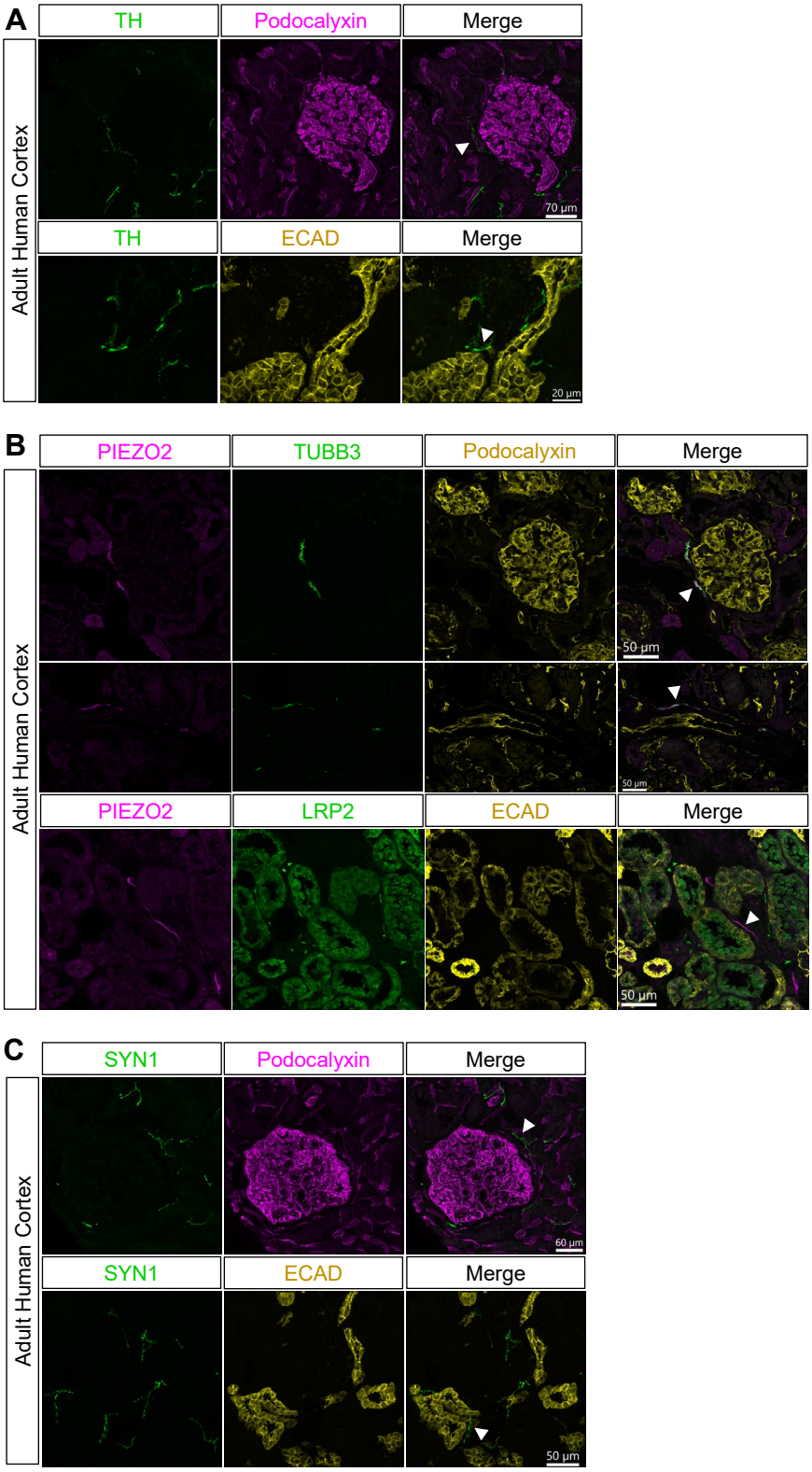
A
TH
Podocalyxin
Merge
Adult Human Cortex
70 µm
TH
ECAD
Merge
20 µm
B
PIEZO2
TUBB3
Podocalyxin
Merge
Adult Human Cortex
50 µm
50 µm
PIEZO2
LRP2
ECAD
Merge
50 µm
C
SYN1
Podocalyxin
Merge
Adult Human Cortex
60 µm
SYN1
ECAD
Merge
50 µm

Figure S1

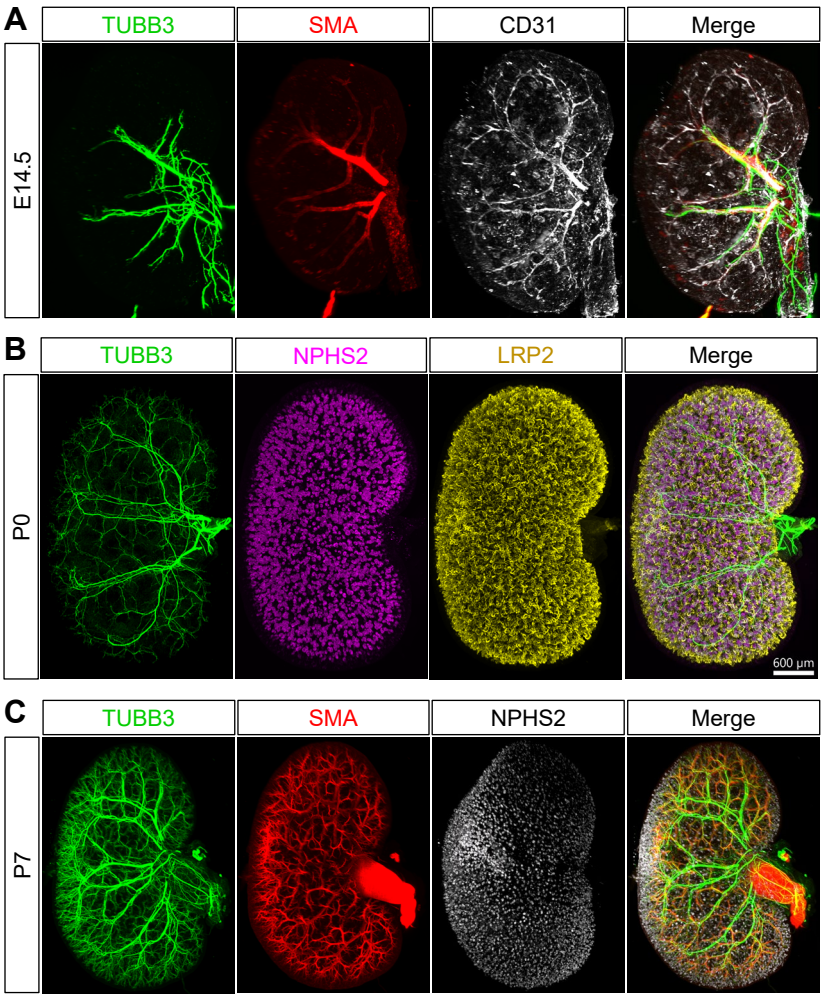
A
TUBB3
SMA
CD31
Merge
E14.5
B
TUBB3
NPHS2
LRP2
Merge
P0
600 µm
C
TUBB3
SMA
NPHS2
Merge
P7

Figure S2

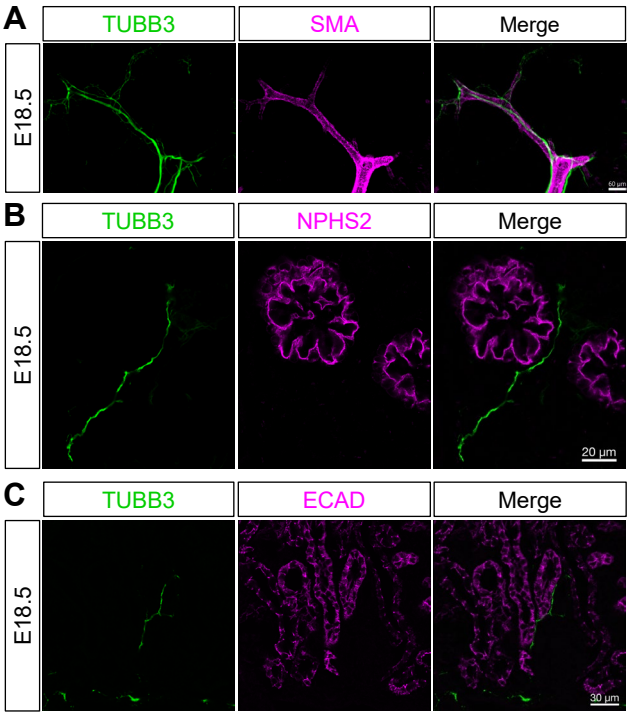
A
TUBB3
SMA
Merge
E18.5
B
TUBB3
NPHS2
Merge
E18.5
20 µm
C
TUBB3
ECAD
Merge
E18.5
30 µm

Figure S3

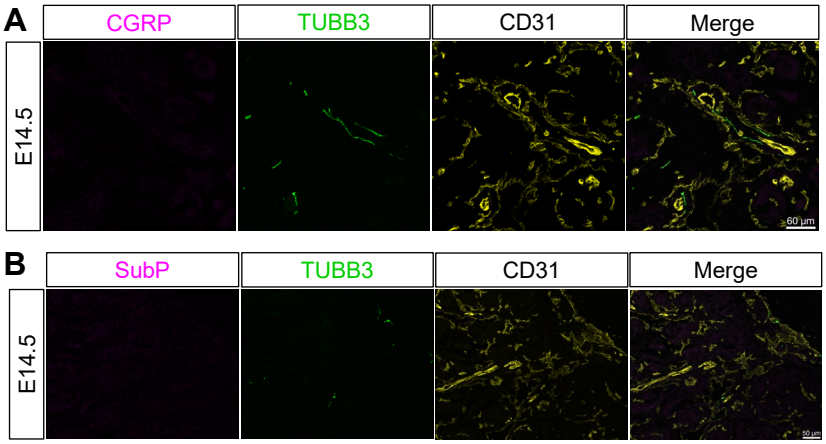
A
CGRP
TUBB3
CD31
Merge
E14.5
60 µm
B
SubP
TUBB3
CD31
Merge
E14.5
50 µm

Figure S4

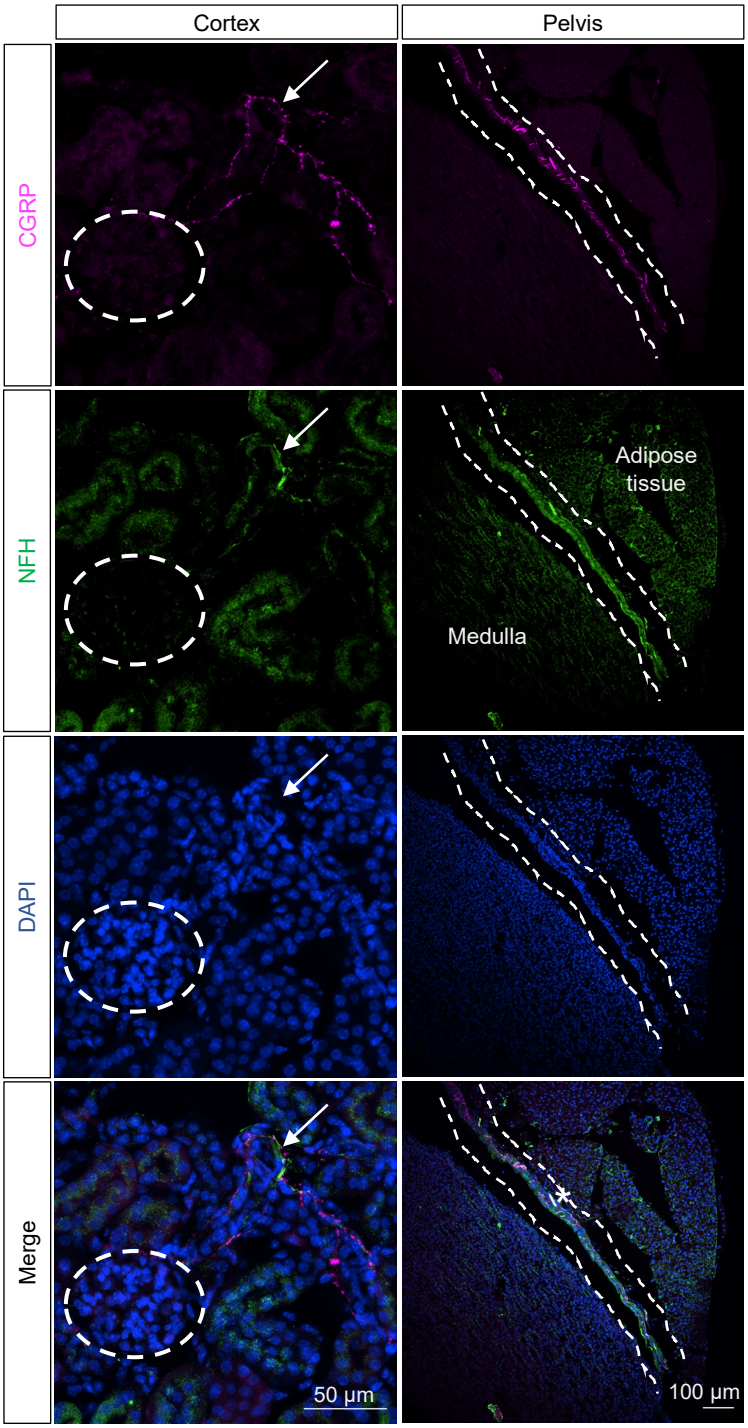
Cortex
Pelvis
CGRP
NFH
DAPI
Merge
Adipose tissue
Medulla
50 µm
100 µm

Figure S5

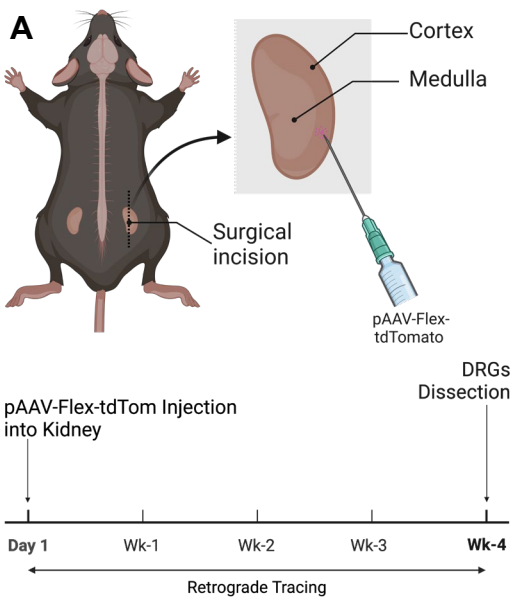
A
Cortex
Medulla
Surgical incision
pAAV-Flex-tdTomato
DRGs Dissection
pAAV-Flex-tdTom Injection into Kidney
Day 1
Wk-1
Wk-2
Wk-3
Wk-4
Retrograde Tracing

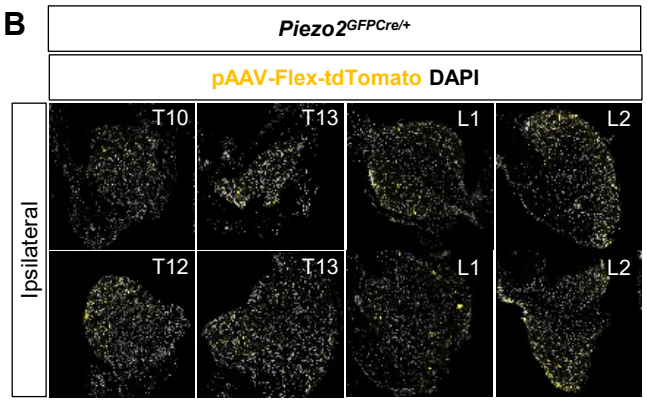
B
Piezo2GFPCre/+
pAAV-Flex-tdTomato DAPI
Ipsilateral
T10
T13
L1
L2
T12
T13
L1
L2

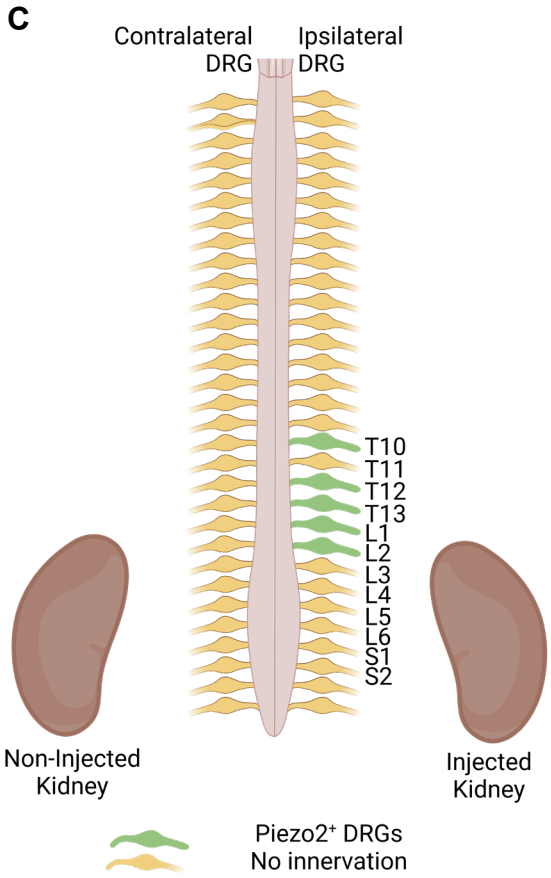
C
Contralateral DRG
Ipsilateral DRG
T10
T11
T12
T13
L1
L2
L3
L4
L5
L6
S1
S2
Non-Injected Kidney
Injected Kidney
Piezo2+ DRGs
No innervation

Figure S6

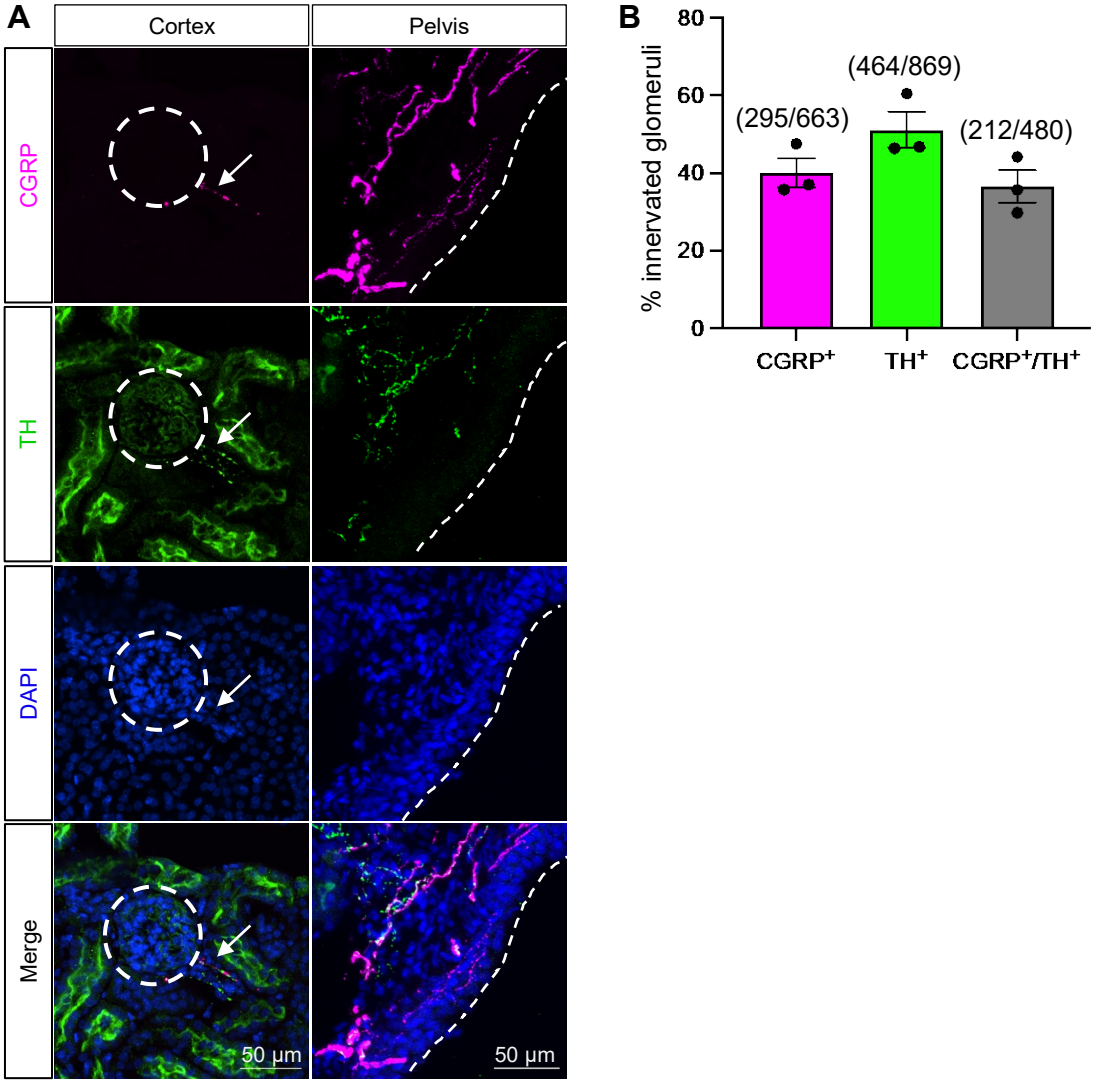
A
Cortex
Pelvis
CGRP
TH
DAPI
Merge
50 µm
50 µm
B
% innervated glomeruli
80
60
40
20
0
(295/663)
(464/869)
(212/480)
CGRP+
TH+
CGRP+/TH+

Figure S7

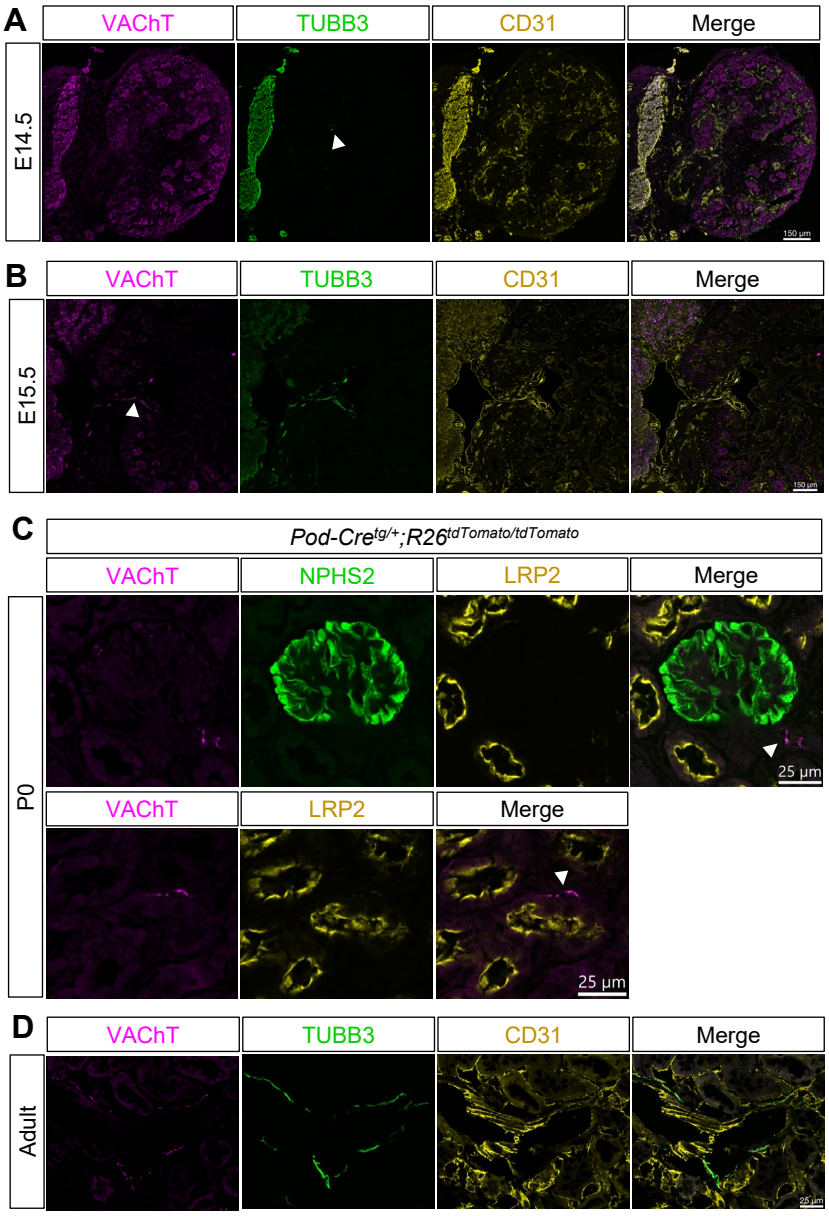
A
VAChT
TUBB3
CD31
Merge
E14.5
150 µm
B
VAChT
TUBB3
CD31
Merge
E15.5
150 µm
C
Pod-Cre tg/+;R26 tdTomato/tdTomato
VAChT
NPHS2
LRP2
Merge
P0
25 µm
VAChT
LRP2
Merge
25 µm
D
VAChT
TUBB3
CD31
Merge
Adult
25 µm

Figure S8

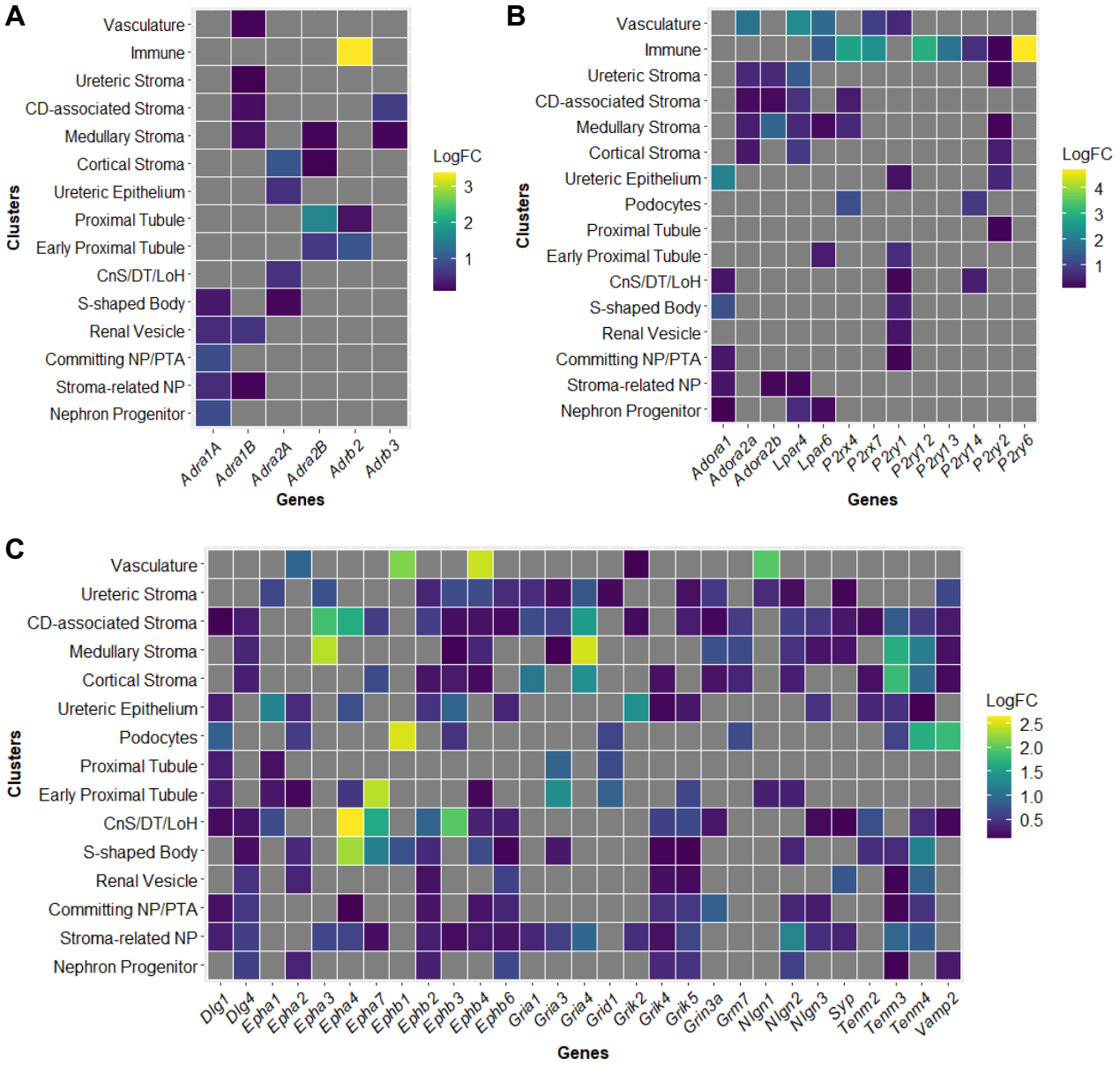
A
Vasculature
Immune
Ureteric Stroma
CD-associated Stroma
Medullary Stroma
Cortical Stroma
Ureteric Epithelium
Proximal Tubule
Early Proximal Tubule
CnS/DT/LoH
S-shaped Body
Renal Vesicle
Committing NP/PTA
Stroma-related NP
Nephron Progenitor
Clusters
Adra1A
Adra1B
Adra2A
Adra2B
Adrb2
Adrb3
Genes
LogFC
3
2
1
B
Vasculature
Immune
Ureteric Stroma
CD-associated Stroma
Medullary Stroma
Cortical Stroma
Ureteric Epithelium
Podocytes
Proximal Tubule
Early Proximal Tubule
CnS/DT/LoH
S-shaped Body
Renal Vesicle
Committing NP/PTA
Stroma-related NP
Nephron Progenitor
Clusters
Adora1
Adora2a
Adora2b
Lpar4
Lpar6
P2rx4
P2rx7
P2ry1
P2ry12
P2ry13
P2ry14
P2ry2
P2ry6
Genes
LogFC
4
3
2
1
C
Vasculature
Ureteric Stroma
CD-associated Stroma
Medullary Stroma
Cortical Stroma
Ureteric Epithelium
Podocytes
Proximal Tubule
Early Proximal Tubule
CnS/DT/LoH
S-shaped Body
Renal Vesicle
Committing NP/PTA
Stroma-related NP
Nephron Progenitor
Clusters
Dlg1
Dlg4
Epha1
Epha2
Epha3
Epha4
Epha7
Ephb1
Ephb2
Ephb3
Ephb4
Ephb6
Gria1
Gria3
Gria4
Grid1
Grik2
Grik4
Grik5
Grin3a
Grm7
Nlgn1
Nlgn2
Nlgn3
Syp
Tenm2
Tenm3
Tenm4
Vamp2
Genes
LogFC
2.5
2.0
1.5
1.0
0.5

Supplementary Table 1

Steps		Modality	Time	Temperature	Volume (mL)
1	Blocking: PBS, 10% (v/v) HISS, 0.5% (v/v) Triton-x 100	passive perfusion on rocker cover from light	1hr	RT	1mL/Kidney pair
2	Primary Antibody Solution: PBS, 10% (v/v) HISS, 0.5% (v/v) Triton-x 100, Primary antibody	passive perfusion on rocker cover from light	7 days	4℃	1mL/Kidney pair
3	Wash Solution: PBS, 0.25% (v/v) Triton-x 100	passive perfusion on rocker cover from light	1 days	RT	1mL/Kidney pair
4	Secondary Antibody Solution: PBS, 10% (v/v) HISS, 0.5% (v/v) Triton-x 100, Secondary antibody	passive perfusion on rocker cover from light	3.5 days	4℃	1mL/Kidney pair
5	Wash Solution: PBS, 0.25% (v/v) Triton-x 100	passive perfusion on rocker cover from light	1 days	RT	1mL/Kidney pair
6	Embed kidneys in 1% Agarose gel to a 5x5mm block	n/a			
7	Methanol Dehydration: 25% (v/v) Methanol in water	passive perfusion on rocker cover from light	1hr	RT	5mL/Kidney pair
8	Methanol Dehydration: 50% (v/v) Methanol in water	passive perfusion on rocker cover from light	1hr	RT	5mL/Kidney pair
9	Methanol Dehydration: 75% (v/v) Methanol in water	passive perfusion on rocker cover from light	1hr	RT	5mL/Kidney pair
10	Methanol Dehydration: 100% (v/v) Methanol	passive perfusion on rocker cover from light	1hr	RT	5mL/Kidney pair
11	DCM Dehydration: 66% (v/v) DCM/33% (v/v) Methanol	passive perfusion on rocker cover from light	3hrs	RT	5mL/Kidney pair
12	DCM Dehydration: 100% (v/v) DCM	passive perfusion on rocker cover from light	15min	RT	5mL/Kidney pair
13	DCM Dehydration: 100% (v/v) DCM	passive perfusion on rocker cover from light	15min	RT	5mL/Kidney pair
14	100% (v/v) DBE Incubation	cover from light	Indefinitly	RT	5mL/Kidney pair

Supplementary Table 2

Figures		System	Objective Specifications						Acquisition/Visualisation Prameters			Data size
			Magnification	NA	RI	WD	Zoom	Total Magnifdication	Image pixel size	Z-step	Note	
Figures												
1	A	UM II	2x; corr.-3.5	0.016	1.56	5.7mm	3.2x	6.4	0.95 µm/pixel	1.4µm	3D recontruction; Maximum intensity projection	47.8 GB
	B	UM II	2x; corr.-3.5	0.016	1.56	5.7mm	2.5x	5.0	1.22 µm/pixel	1.4µm	3D recontruction; Maximum intensity projection	38.8 GB
	C	UM II	2x; corr.-3.5	0.016	1.56	5.7mm	4x	8.0	0.75 µm/pixel	1.4µm	3D recontruction; Maximum intensity projection	40.0 GB
	D	UM II	2x; corr.-3.5	0.016	1.56	5.7mm	2.5x	5.0	1.22 µm/pixel	1.4µm	3D recontruction; Maximum intensity projection	59.8 GB
2	A	UM II	2x; corr.-3.5	0.016	1.56	5.7mm	4x	8.0	0.75 µm/pixel	1.4µm	3D recontruction; Maximum intensity projection	55.9 GB
	B	LSM 880	20x	0.8	1.0	0.55mm	n.a	20	0.12 µm/pixel	n.a	2D single slice	40.28 MB
	C	LSM 880	20x	0.8	1.0	0.55mm	n.a	20	0.12 µm/pixel	7.9µm	3D recontruction; Maximum intensity projection	360.88 MB
3	A	LSM 880	20x	0.8	1.0	0.55mm	n.a	20	0.12 µm/pixel	n.a	Tile Scan 2x2; 2D single slice	160.53 MB
	B	LSM 900	40x oil	1.4	1.51	0.13mm	n.a	40	0.07 µm/pixel	n.a	Tile Scan 3x3; 2D single slice	454.14 MB
	C	LSM 880	40x oil	1.3	1.51	0.21mm	n.a	40	0.08 µm/pixel	n.a	2D single slice	59.81 MB
	D	LSM 880	40x oil	1.3	1.51	0.21mm	n.a	40	0.08 µm/pixel	n.a	2D single slice	26.68 MB
	E	LSM 880	40x oil	1.3	1.51	0.21mm	n.a	40	0.08 µm/pixel	n.a	Tile Scan 2x2; 2D single slice	106.24 MB
	F	LSM 880	40x oil	1.3	1.51	0.21mm	n.a	40	0.08 µm/pixel	n.a	Tile Scan 2x2; 2D single slice	106.23 MB
	G	LSM 900	40x oil	1.4	1.51	0.13mm	n.a	40	0.07 µm/pixel	n.a	2D single slice	40.17 MB
4	B	LSM 780	20x	0.8	1.0	0.55mm	0.6	20x	0.69 µm/pixel	n.a	2D single slice	4226 KB
	C	DMi8	20x DMi8	0.4	1.0	6.2-7.5 mm	n.a	20x	0.32 µm/pixel	n.a	2D single slice, Ipsilateral kidney image	38.1 MB
		DMi8	20x DMi8	0.4	1.0	6.2-7.5 mm	n.a	20x	0.32 µm/pixel	n.a	2D single slice, Cintralateral kidney image	36.6 MB
5	A											
	B	UM II	2x; corr.-3.5	0.016	1.56	5.7mm	2x	4	1.54 µm/pixel	2.0µm	3D recontruction; Maximum intensity projection	49.2 GB
	C	LSM 880	40x oil	1.3	1.51	0.21mm	n.a	40	0.08 µm/pixel	n.a	2D single slice	26.68 MB
	D	LSM 900	40x oil	1.4	1.51	0.13mm	n.a	40	0.07 µm/pixel	n.a	2D single slice	40.17 MB
	E	LSM 900	40x oil	1.4	1.51	0.13mm	n.a	40	0.07 µm/pixel	n.a	Tile Scan 2x2; 2D single slice	203.39 MB
6	A	LSM 880	20x	0.8	1.0	0.55mm	n.a	20	0.12 µm/pixel	n.a	2D single slice	144.91 MB
		LSM 880	40x oil	1.3	1.51	0.21mm	n.a	40	0.08 µm/pixel	n.a	2D single slice	26.68 MB
	B	LSM 880	20x	0.8	1.0	0.55mm	n.a	20	0.12 µm/pixel	0.90µm	3D recontruction; Maximum intensity projection	361.31 MB
		LSM 880	40x oil	1.3	1.51	0.21mm	n.a	40	0.08 µm/pixel	0.50µm	Tile Scan 2x2; 3D recontruction; Maximum intensity projection	3.11 GB
	C	LSM 880	20x	0.8	1.0	0.55mm	n.a	20	0.12 µm/pixel	0.90µm	3D recontruction; Maximum intensity projection	920.56 MB
7	A	LSM 880	40x oil	1.3	1.51	0.21mm	n.a	40	0.08 µm/pixel	1.8µm	Tile Scan 3x3; 3D recontruction; Maximum intensity projection	3.96 GB
	B	LSM 880	40x oil	1.3	1.51	0.21mm	n.a	40	0.08 µm/pixel	n.a	Tile Scan 2x2; 2D Single slice	106.23 MB
		LSM 880	40x oil	1.3	1.51	0.21mm	n.a	40	0.08 µm/pixel	n.a	Tile Scan 3x2; 2D Single slice	159.22 MB
		LSM 880	40x oil	1.3	1.51	0.21mm	n.a	40	0.08 µm/pixel	0.54µm	Tile Scan 2x2; 3D recontruction; Maximum intensity projection	2.9 GB
	C	LSM 880	40x oil	1.3	1.51	0.21mm	n.a	40	0.08 µm/pixel	1.8µm	Tile Scan 3x3; 3D recontruction; Maximum intensity projection	3.73 GB
		LSM 880	40x oil	1.3	1.51	0.21mm	n.a	40	0.08 µm/pixel	0.95µm	Tile Scan 2x2; 3D recontruction; Maximum intensity projection	2.17 GB
Sup. Figures												
S1	A	UM II	2x; corr.-3.5	0.016	1.56	5.7mm	3.2x	6.4	0.95 µm/pixel	1.4µm	3D recontruction; Maximum intensity projection	38.2 GB
	B	UM II	2x; corr.-3.5	0.016	1.56	5.7mm	1.6x	3.2	1.95 µm/pixel	2.0µm	3D recontruction; Maximum intensity projection	56.5 GB
	C	UM II	2x; corr.-3.6	0.016	1.56	5.7mm	2x	4	1.54 µm/pixel	2.0µm	3D recontruction; Maximum intensity projection	54.2 GB
S2	A	A.D. SDC	25x	0.95	1.33	2.4mm	n.a	25x			3D recontruction; Maximum intensity projection	4.82 GB
	B	LSM 880	40x oil	1.3	1.51	0.21mm	n.a	40	0.08 µm/pixel	n.a	2D single slice	26.29 MB
	C	LSM 880	40x oil	1.3	1.51	0.21mm	n.a	40	0.42 µm/pixel	n.a	Tile Scan 2x2; 2D single slice	8.2 MB
S5	B	LSM 780	20x	0.8	1.0	0.55mm	0.6	20x	0.69 µm/pixel	n.a	2D single slice	4226 KB
S7	A	LSM 880	20x	0.8	1.0	0.55mm	n.a	20	0.83 µm/pixel	n.a	Tile Scan 3x3; 2D single slice	18.22 MB
	B	LSM 880	20x	0.8	1.0	0.55mm	n.a	20	0.83 µm/pixel	n.a	Tile Scan 3x3; 2D single slice	18 MB
	C	LSM 880	40x oil	1.3	1.51	0.21mm	n.a	40	0.08 µm/pixel	n.a	2D single slice	26.7 MB
		LSM 880	40x oil	1.3	1.51	0.21mm	n.a	40	0.08 µm/pixel	n.a	Tile Scan 2x2; 2D single slice	106.23 MB
	D	LSM 880	40x oil	1.3	1.51	0.21mm	n.a	40	0.08 µm/pixel	n.a	Tile Scan 2x2; 2D single slice	100 MB

Legend of abbreviations

Imaging Systems

UM II	LaVision BioTec - UltraMicroscope II
LSM 880	Zeiss confocal LSM880 with Airyscan
LSM 900	Zeiss confocal LSM900
A.D. SDC	Andor Dragonfly Spinning Disk Confocal
DMi8	Leica DMi8 Inverted Fluorescent Microscope
LSM 780	Zeis confocal LSM 780
NA	Numerical aperture
RI	Refractive index
WD	Working distance
n.a.	not applicable

Objectives

2x corr.	Olympus MVPLAPO 2X/0.5; correction colar 3.5
20x	Plan-Apo 20x/0.8WD 0.55mm
20x DMi8	HC PL Fluotar L M25
40x	Plan-Neofluar 40x/1.3 oil WD0.21
40x	40X/0.6 LD Plan Neo

Supplementary Table 3

Antibody	Vendor	Cat #	Host	Dilution IF	Dilution WM	Alternate name, labels
CD31	BD Pharmingen	550274	Rat	1:100	1:50	Pecam1, Endothelial cell
CGRP	Immunostar	24112	Rabbit	1:250	n/a	Calcitonin Gene-Related Peptide, Peptidergic sensory nerve
CytoK	Sigma-Aldrich	C2931-.2ML	Mouse IgG1	1:500	1:250	Cytokeratin, Ureteric tree
ECAD	Invitrogen	131900	Rat	1:500	1:250	E-cadherin, Tubule epithelium
LRP2	MyBiosource	MBS690201	Mouse IgG1	1:500	1:250	Megalin, Proximal tubule
NFH	Abcam	AB4680	Chicken	1:1000	n/a	Neurofilament heavy polypeptide,
NPHS2	Invitrogen	PA579757	Rabbit	1:500	1:250	Podocin, Podocytes, Glomeruli
NPY	Novus Biologicals	NBP1-46535SS	Chicken	1:250	n/a	Neuropeptide Y, Sympathetic nerve
PIEZO2	Novus Biologicals	NBP1-78624	Rabbit	1:250	n/a	Mechanosensitive sensory nerve
PIEZO2	Novus Biologicals	NBP1-78538	Rabbit	1:250	n/a	Mechanosensitive sensory nerve
PODXL	R&D Systems	AF1658	Goat	1:500	1:250	Podocalyxin, glomeruli, endothelium
SMA-488	Invitrogen	53-9760-82	Mouse IgG2a	1:500	1:250	Smooth muscle actin, Arterial tree
SubP	Immunostar	20064	Rabbit	1:100	n/a	Substance P Peptidergic sensory nerve
SYN1	Invitrogen	51-5200	Rabbit	1:1000	n/a	Synapsin I, Synaptic vesicle marker
TH	Milipore Sigma	AB152	Rabbit	1:500	1:250	Tyrosine Hydroxylase Noradrenergic sympathetic nerve
TH	Abcam	AB76442	Chicken	1:250	n/a	Tyrosine Hydroxylase Noradrenergic sympathetic nerve
TUBB3	BioLegend	801202	Mouse IgG2a	1:500	1:250	Class 3 Tubulin Pan-neuronal marker
TUBB3-594	BioLegend	801208	Mouse IgG2a	1:500	1:250	Class 3 Tubulin Pan-neuronal Marker
VAChT	SySy	139105	Guinea-Pig	1:100	n/a	Vesicular acetylcholine transporter, Parasympathetic (Cholinergic) nerve
RFP	Rockland	600901379	Chicken	1:500	1:250	Recombinant RFP (tdTomato)